Electronic Supplementary Material

Spin polarization strategy to deploy proton resource over atomic-level metal sites for highly selective CO_2 electrolysis

Yingjie Zhao[1], Xinyue Wang[1], Xiahan Sang[3], Sixing Zheng[1], Bin Yang[1,2],
Lecheng Lei[1,2], Yang Hou[1,2], Zhongjian Li (✉)[1,2]

1 Key Laboratory of Biomass Chemical Engineering of Ministry of Education, College of Chemical and Biological Engineering, Zhejiang University, Hangzhou 310027, China

2 Institute of Zhejiang University-Quzhou, Quzhou 324000, China

3 Nanostructure Research Centre, Wuhan University of Technology, Wuhan 430070, China

E-mail: zdlizj@zju.edu.cn

Table of Contents

Theoretical Computation

Text S1. Structural optimization was performed by first-principle calculations within density functional theory (DFT) framework, as implemented in the plane-wave basis set Vienna *ab initio* Simulation Package (VASP) code [1,2]. Exchange-correlation energy was modelled by Perdew-Burke-Ernzerhof (PBE) functional using generalized gradient approximation (GGA) [3]. The interactions between the valence electrons and the ionic cores were described by projector augmented wave (PAW) pseudo-potentials [4]. Cutoff energy of 400 eV was selected after a series of tests. It is widely recognized that the correlation between the localized 3*d* electrons in fourth-period transition metals can be divided into on-site coulomb (U) and exchange (J) interactions, a key element of $\mathrm{DFT}+U$ method. Here the $\mathrm{DFT}+U$ was employed through rotationally invariant approach [5], setting the value of U-J parameter being 3.29 suitable for Fe, consistent with previous theoretical work [6]. Van der Waals force was considered for dispersion corrections based on DFT-D3 method [7]. Convergence threshold for the iteration (ionic relaxations) in self-consistent field (SCF) was set at 10^{-5} eV, and that for geometry optimizations by BFGS algorithm was set to be 0.02 eV Å^{-1} on maximum force component. A Monkhorst-Pack *k*-point mesh of 2 × 2 × 1 was used to perform geometry optimizations. Top three layers were fully relaxed during structural optimization when the others were fixed at the tested lattice positions.

Experimental Section

Chemicals and Reagents

Text S2. Hemin ($C_{34}H_{32}ClN_4O_4Fe$) was purchased from Heowns Biochem Technologies. LLC. Tianjin. Melamine, pyromellitic acid and carbon black (VXC-72) were purchased from Shanghai Macklin Biochemical Co., Ltd. $Fe(NO_3)_3{\cdot}9\,H_2O$, methanol and ethanol were purchased from Sinopharm Chemical Reagent Co., Ltd. All the chemicals were analytical reagents as directly used without additional purification. Deionized water (ρ > 18 MΩ·cm) was used in all experiments.

Catalyst Synthesis

Text S3. *Synthesis of Fe_3C-X@Fe-NC series*: The preparation followed a previously reported method with some modification [8]. In a typical synthesis, hemin (0.326 g, 0.5 mmol) and melamine (5.0 g) were mixed in methanol (250 mL) and stirred for 18 h at room temperature. The methanol was subsequently removed by vacuum distillation using rotary evaporator and a brown powder was obtained. This precursor was loaded into a capped porcelain boat and placed into a tube furnace. The pyrolysis was carried out under N_2 atmosphere with a three-stage heating program: 20 to 180 ℃, 180 to 360 ℃ and 360 to x ℃ (x = 900, 1000 and 1100 for Fe_3C-S@Fe-NC,

Fe_3C-M@Fe-NC and Fe_3C-L@Fe-NC, respectively); each stage divides into a ramping (rate: 2 ℃ min^{-1}) and an isothermal (holding time: 2 h) step. The catalyst was finally obtained as a black powder.

Text S4. *Synthesis of Fe-NC*: Fe-NC was prepared using the same procedure as the Fe_3C-X@Fe-NC series except for the final calcination temperature x = 800.

Text S5. *Synthesis of FeC@C*: The Fe_3C-contained composite was prepared by following a previous work [9]. In a typical synthesis, carbon black (100 mg) was immersed into an aqueous solution (60 mL) with dissolved $Fe(NO_3)_3 \cdot 9\,H_2O$ (60 mg), and then ultrasonicated for 2 h and vigorously stirred overnight. The water was subsequently removed by rotary evaporation. A brownish black powder was collected and put into a porcelain boat before being transferred to a tube furnace. The pyrolysis procedure was set the same as Fe_3C-L@Fe-NC except that the atmosphere was a mixed gas of N_2 and CO with inflow rates of 2:1.

Text S6. *Synthesis of NC*: The method in a previous report was referred to to prepare NC containing neither atomic Fe nor nanostructured Fe_3C [10]. In a typical synthesis, pyromellitic acid (4.575 g, 18 mmol) and melamine (3.027 g, 24 mmol) were mixed in deionized water (200 mL) inside a glass bottle and vigorously stirred for 18 hours at room temperature. The bottle was subsequently sealed with a plastic cap and put into an air-flow oven operated at 110 ℃ for 12 hours. The resulting precipitate was collected and then dried under vacuum at 60 ℃ overnight. The as-prepared white product was ground into powder and then pyrolyzed under N_2 atmosphere with the same procedure as Fe_3C-L@Fe-NC to obtain NC.

Structure Characterization

Text S7. The morphologies and microstructures were observed by transmission electron microscopy (TEM), high-resolution TEM (HR-TEM) (JEM-2100F, JEOL) and aberration-corrected high-angle annular dark-field scanning transmission electron microscopy (AC-HAADF-STEM) (Titan Cubed Themis G2 300, Thermo Fisher Scientific). X-ray diffraction (XRD) spectra were recorded on powder X-ray diffractometer (X-pert Powder, PANalytical B.V.). X-ray photoelectron spectroscopy (XPS) measurements were performed on Escalab 250Xi system (Thermo Fisher Scientific), equipped with a monochromatic Al Kα radiation source. Inductively coupled plasma mass spectrometry (ICP-MS) measurements were performed on Agilent 7700x (Agilent Technologies). Thermogravimetry (TG) analyses were performed on thermal analyzer (SDT Q600, TA Instruments).

Preparation of Working Electrode

Text S8. The as-prepared catalyst (10 mg) was ultrasonically dispersed into a mixed solution containing ethanol-water (4:1, V/V, 900 μL) and 0.5 wt.% Nafion (100 μL), and then vigorously stirred overnight to obtain a uniform ink. The ink was dropwise coated carefully onto a carbon paper sized 1 cm × 3 cm as working electrode. The geometric area of catalyst was 1 cm^2 with loading amount of 1 mg cm^{-2}.

Electrochemical Measurements

Text S9. Electrochemical measurements were first performed on electrochemical analyzer (CHI 760E, CH Instruments) in a three-electrode H-cell filled with 0.5 M $KHCO_3$ electrolyte. Working (catalyst) and reference (Ag/AgCl; saturated KCl solution) electrodes were fixed in cathodic chamber and the counter electrode (Pt wire) was fixed in anodic chamber. Two chambers were separated by a Nafion 117 membrane to ensure proton exchange and prevent electrolyte crossover. All the potentials used in the main text and Supporting Information are corrected by Nernst equation and vs. reversible hydrogen electrode (RHE; $E_{\mathrm{RHE}} = E + 0.0591 \times \mathrm{pH} + 0.197$ V, at 25 °C). Before and during the tests of electrocatalytic CO_2RR, the cell was bubbled with CO_2 (99.99%) flow at 20 sccm continuously to saturate the electrolyte. After cyclic voltammogram (CV; scan rate: 50 mV s^{-1}) activation until the catalyst ran steadily over the potential ranging from 0 to −1.2 V, linear sweep voltammetry (LSV; scan rate: 5 mV s^{-1}) polarization curve was recorded over the same potential window. The CV curves for electrochemical active surface area (ECSA) calculation were collected from 0.54 to 0.64 V at varying scan rates. Electrochemical impedance spectroscopy (EIS) measurement was conducted by applying −0.4 V with 100 mV amplitude over a frequency range from 100 kHz to 0.1 Hz. Gas products were monitored by on-line gas chromatography (GC) equipped with flame ionization detector (FID) for CO and thermal conductivity detector (TCD) for H_2 quantification. Liquid product was detected by off-line ^{1}H NMR (Agilent DD2 600 MHz, Agilent Technologies), which had been continuously accumulated until the total charge for reduction reached 1 C. Dimethyl sulfoxide (DMSO) was added into the electrolyte sample as inner standard. Tafel slope was calculated according to Tafel equation (η = a + blog(j_{CO}), where η is overpotential; b is Tafel slope; j_{CO} is partial current density of CO). To carry out poisoning experiment, 1 M KSCN were added into the electrolyte. Electrochemical OER tests were carried out in CO_2-saturated 0.8 M $KHCO_3$ electrolyte to simulate the operating condition of Zn–CO_2 battery charging process (see below). OER LSV polarization curve was recorded at scan rate of 5 mV s^{-1}.

In Situ ATR-SEIRAS

Text S10. In situ attenuated total reflectance surface enhanced infrared absorption spectroscopy (ATR-SEIRAS) is a powerful tool for detecting the adsorbed substances or functional groups on catalyst's surface. ATR-SEIRAS experiment was performed on Bruker INVENIO R FT-IR spectrometer equipped with a variable angle ATR sampling accessory and a MCT (Hg/Cd/Te) detector cooled by liquid nitrogen. A Si face-angled crystal with incident angle of 60° was used as reflection element. Then an ultrathin Au foil was chemically deposited on the Si crystal for IR signal enhancement and electron conduction. Electrocatalyst (loading amount: 0.1 mg cm^{-2}) was evenly coated onto the Au film to serve as working electrode. Pt rod and Ag/AgCl were used as counter and reference electrodes, respectively. CO_2-saturated 0.5 M $KHCO_3$ was used as electrolyte. The in situ SEIRAS spectra were collected during the chronopotentiometry tests at varying applied potentials (−1.0 to 0 V with a step interval of 0.1 V). The spectral resolution was set at 4 cm^{-1} and 32 interferograms were co-added for each spectrum. The spectra are given in absorbance unit defined as Abs. = $-\lg(R/R_0)$, where R and R_0 (the intensity of IR signal measured at 0 V was used as R_0) are the reflected IR intensity corresponding to sample- and reference-single beam spectra, respectively.

Assembly of Flow Cell

Text S11. In flow cell operation, a three-electrode and three-compartment device was used. Catalyst-loaded gas diffusion electrode (GDE), nickel foam and Ag/AgCl served as cathode, anode and reference, respectively. 1.5 M $KHCO_3$ electrolyte pre-saturated with argon was injected into the cathodic and anodic chambers that were separated by an anion-exchange membrane (FAB-PK-130). CO_2 gas at 20 sccm was delivered into the gas chamber and flowed through the backside of the GDE. Working area of the GDE is 1 cm^2 coated with catalyst. The device was operated in galvanostatic mode; each steady-state current point along with the corresponding potential and FE_{CO} was recorded.

Assembly of Aqueous Rechargeable Zn–CO_2 Battery

Text S12. Aqueous rechargeable Zn–CO_2 battery (ZCB) was assembled using a double-chamber square cell, injected with anolyte (0.2 M $Zn(CH_3COO)_2$ + 6 M KOH) and catholyte (near-neutral 0.8 M $KHCO_3$), respectively. A bipolar membrane was applied to prevent cross-contamination caused by mass transfer between the compartments and to maintain the respective pH of the two different electrolytes. Clean Zn foil plate (2 cm × 4 cm; pretreated by acid to etch off the possible oxide layer) and carbon paper coated with appropriate amount of iron catalyst (1 mg cm^{-2}) served as anode and cathode, respectively. CO_2 gas flowed through the cathodic compartment at 20 sccm in all tests, and gas products were monitored by GC. Discharge/charge polarization curves and discharge/charge voltage plots were recorded using LSV and constant-current techniques, respectively, on electrochemical workstation (CHI 760E, CH Instruments). Long-term galvanostatic discharge/charge cycling was performed on battery testing system (CT-4008T, NEWARE).

Calculation Methods

Quantification of Atomic and Nanostructured Iron

Text S13. During TG measurement under air atmosphere, all the Fe species in the catalyst were oxidized and transformed into Fe_2O_3. Total Fe content ($\mathrm{Total_{Fe}}$) of the sample is calculated based on the mass of Fe_2O_3:

$$\mathrm{Total_{Fe}} = \frac{2 \times M_{\mathrm{Fe}} \times m_{\mathrm{Fe_2O_3}}}{M_{\mathrm{Fe_2O_3}} \times m_{\mathrm{cat.}}} \times 100\%$$

Where M_{Fe} and $M_{\mathrm{Fe_2O_3}}$ are the molecular weight of Fe and Fe_2O_3, respectively; $m_{\mathrm{cat.}}$ and $m_{\mathrm{Fe_2O_3}}$ are the mass of the catalyst and the Fe_2O_3 obtained after TG, respectively.

For Fe-NC with no crystalline iron, the content of atomic Fe respectively quantified by TG and ICP agreed well with each other. On the basis of the fact that most of the nanostructured Fe_3C was entirely wrapped and protected by several highly ordered graphitic layers in Fe_3C-X@Fe-NCs, and thus resistant to strong acid solution used for ICP detection, the content of Fe given by ICP could be ascribed to atomic Fe, and that of nanostructured Fe_3C could be calculated by deducting the atomic Fe part from the total Fe given by TG:

$$\mathrm{Nanostructured_{Fe_3C}} = \mathrm{Total_{Fe}} - \mathrm{Atomic_{Fe}}$$

Finally, ratio of nanostructured Fe_3C vs. atomic Fe ($\mathrm{N_{Fe}/A_{Fe}}$) was defined to describe the configuration of the A/N-Fe pairs in Fe_3C-X@Fe-NC series:

$$\mathrm{N_{Fe}/A_{Fe}} = \frac{\text{Nanostructured Fe}_3\text{C}}{\text{Atomic Fe}}$$

Faradic Efficiency of Gaseous Product

Text S14. According to the definition of Faradic efficiency:

$$\mathrm{FE_g} = \frac{Q_{\mathrm{g}}}{Q_{\mathrm{total}}} = \frac{z_{\mathrm{g}} n_{\mathrm{g}} F}{It}$$

Where n_{g} is moles of product g (g = CO or H_2); z_{g} is number of the electrons required to produce one g molecule, which is 2 for CO and H_2; I is stable current of the chronoamperometry test; F is Faradaic constant (96485 C $\mathrm{mol^{-1}}$).

Based on the GC data and ideal gas law:

$$n_{\mathrm{g}} = x_{\mathrm{g}} \times n_{\mathrm{total}}$$

$$n_{\mathrm{total}} = \frac{pV_{\mathrm{o}}}{RT}$$

$$V_{\mathrm{o}} = f \times t$$

Where x_{g} is faction of the gas g detected by GC; n_{total} is moles of all the gases; V_{o} is volume of all the gases; f is volumetric flow rate; p is atmospheric pressure (101.3 kPa); T is ambient temperature (298 K); R is ideal gas constant (8.314 J mol^{-1} K^{-1}).

Finally, Faradaic efficiencies of CO and H_2 (FEg, g = CO or H_2) were calculated from the equation below:

$$\text{FE}_\text{g} = \frac{z_\text{g} r_\text{g} F}{I} = \frac{z_\text{g} x_\text{g} f p F}{IRT}$$

Where r_g is generation rate of gas g. All the error bars for FE_CO were based on the tests of three individual working electrodes loaded with three individual batches of a specific catalyst.

Evaluation of Turnover Frequency

Text S15. Partial current density of CO (J_CO) was calculated according to:

$$J_\text{CO} = J \times \text{FE}_\text{CO}$$

TOFs for the CO_2RR were calculated based on the 2-electron pathway of CO_2-to-CO:

$$\text{TOF} = \frac{\text{Turnover number for CO production}}{\text{Number of active sites}}$$

Turnover number of CO production:

$$\text{TON} = \frac{Q \times \text{FE}_\text{CO}}{2F} N_\text{A} = \frac{J_\text{CO} \times t}{2F} N_\text{A}$$

Where Q is the total charge consumed; t is time (3600 s); F is Faradaic constant (96485 C mol^{-1}); N_A is Avogadro constant (6.02×10^{23}).

Number of active sites:

$$\text{N} = \frac{m \times w\%}{M} N_\text{A}$$

Where m is loading amount of the catalyst; $w\%$ is weight fraction of atomic Fe in the catalyst; M is relative atomic mass of Fe. Assuming that all the isolated Fe sites were catalytically active centers for CO_2RR, TOFs were calculated from the equation below:

$$\text{TOF (h}^{-1}\text{)} = \frac{\text{TON}}{\text{N}} = \frac{J_\text{CO} / 2F}{m w\% / M} \times 3600$$

Fitting of ECSA

Text S16. ECSA was measured to evaluate the accessible surface area utilized by CO_2RR. According to the definition:

$$\text{ECSA} = \frac{C_\text{dl}}{C_\text{s}}$$

Where C_dl is double layer capacitance, estimated by slope of the plot of the difference (Δj) between double-layer charging (j_c) and discharging (j_d) current density ($\Delta j = (j_\text{c} - j_\text{d}) / 2$) vs. the scan rate; C_s is specific capacitance, the value of which is assumed to be 20 μF cm^{-2} by regarding the C_dl per cm^2 of electrochemical surface area of the catalyst as identical to that of graphene.

Mass-normalized ECSA (ECSA_m) was finally obtained:

$$\mathrm{ECSA}_m = \frac{\mathrm{ECSA}}{m}$$

Where m is loading amount of the catalyst per cm^2.

CO Production

Text S17. Production rate of CO (r_{CO}) was calculated according to:

$$r_{\mathrm{CO}} = \frac{I \times \mathrm{FE}_{\mathrm{CO}}}{z_{\mathrm{CO}} F}$$

Where I is steady-state current on the GDE; z_{CO} is number of the electrons required to produce a CO molecule; F is Faradaic constant (96485 C mol^{-1}).

Mole production of CO (n_{CO}):

$$n_{\mathrm{CO}} = r_{\mathrm{CO}} \times t$$

Where t is interval time.

Standardized volume production of CO (V_{CO}), according to ideal gas equation:

$$V_{\mathrm{CO}} = \frac{n_{\mathrm{CO}} RT}{p}$$

Where R is ideal gas constant (8.314 J mol^{-1} K^{-1}); T is ambient temperature (298 K); p is atmospheric pressure (101.3 kPa).

Power Density of Zn–CO_2 Battery

Text S18. According to the definition of power, electric work per unit time (P) delivered by Zn–CO_2 battery was calculated by:

$$P = I \times V$$

Where I and V are discharging current and voltage of the battery, respectively. The powder density was finally normalized by geometric working area.

Figures

DFT Calculations

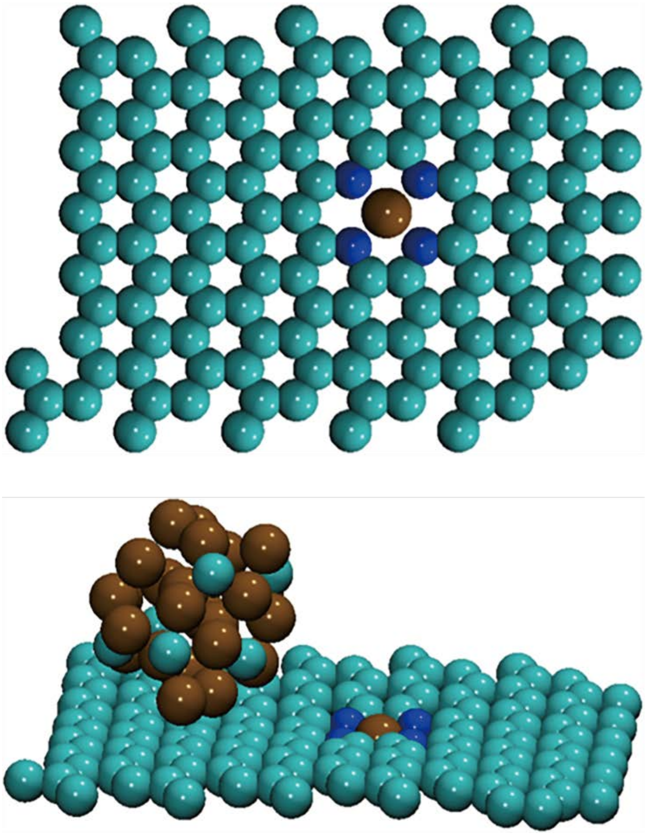

Fig. S1 Geometric models of SA-Fe (top) and A/N-Fe (bottom). Fe atom: brown ball; N: blue; C: cyan.

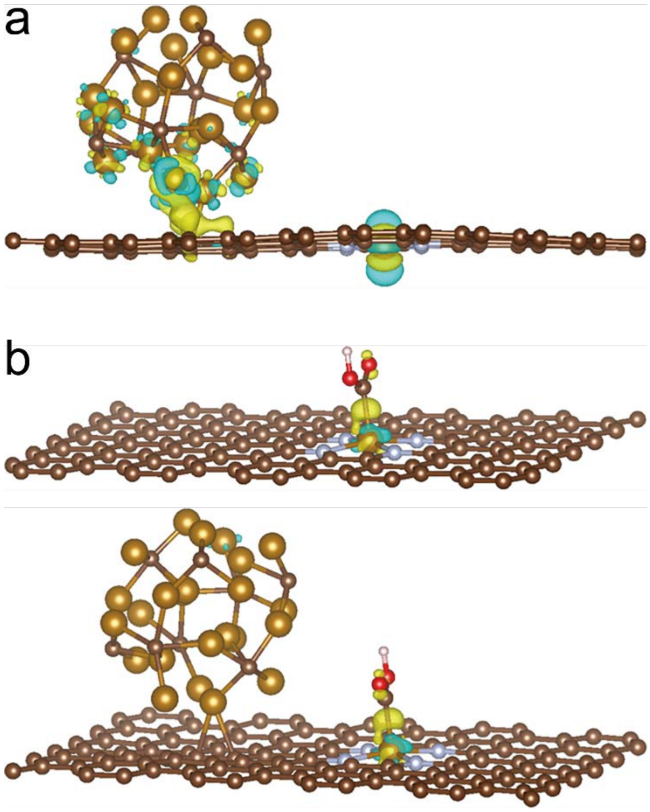

Fig. S2 (a) Differential charge density for A/N-Fe. Build-up and depletion of charge are marked by yellow and sky-blue colors, respectively. There exists a noticeable charge migration from the Fe_3C to the contacting *sp*^{2} C, characteristic of the interfacial interaction between Fe^0 species and graphene [11]. (b) Charge density difference mappings for the *COOH generation step on the catalytic Fe site of SA-Fe (top) and A/N-Fe (bottom). Electron domain appears in the Fe-C bonding region during the reaction. The number of outermost electrons calculated by Bader charge analysis in C atom of the *COOH outside A/N-Fe is 2.71, slightly larger than the case of SA-Fe (2.69), implying that A/N-Fe is superior to SA-Fe in electron donation to better prepare the intermediates for further protonation.

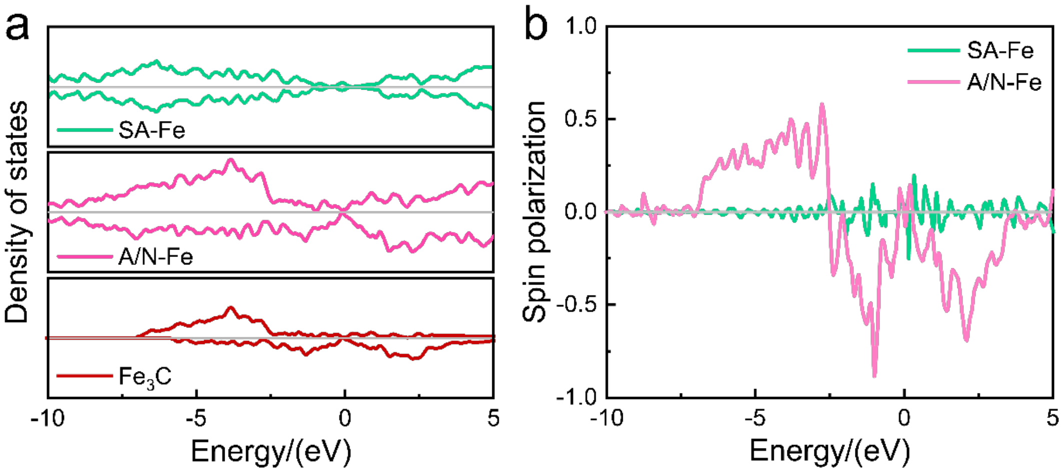

Fig. S3 (a) Total DOS of SA-Fe, A/N-Fe, and Fe_3C. The upper and lower panels are for spin-up and -down channels, respectively. (b) Spin polarization ratio (SPR) of SA-Fe and A/N-Fe. SPR is defined as the difference between majority of and minority of DOS normalized by the overall DOS at a certain energy level, i.e., $SPR(E) = [DOS_{\uparrow}(E) - DOS_{\downarrow}(E)] / [DOS_{\uparrow}(E) + DOS_{\downarrow}(E)]$ [12]. Positive (negative) sign of the SPR indicates up (down) polarization orientation of the electronic states. Unlike the neutral spins in SA-Fe, the SPR of which just oscillates around zero position, striking positive and negative values appear at the low- and high-energy side in A/N-Fe, respectively, in accord with the polarization picture induced by the phenomenon of exchange splitting (Scheme S1).

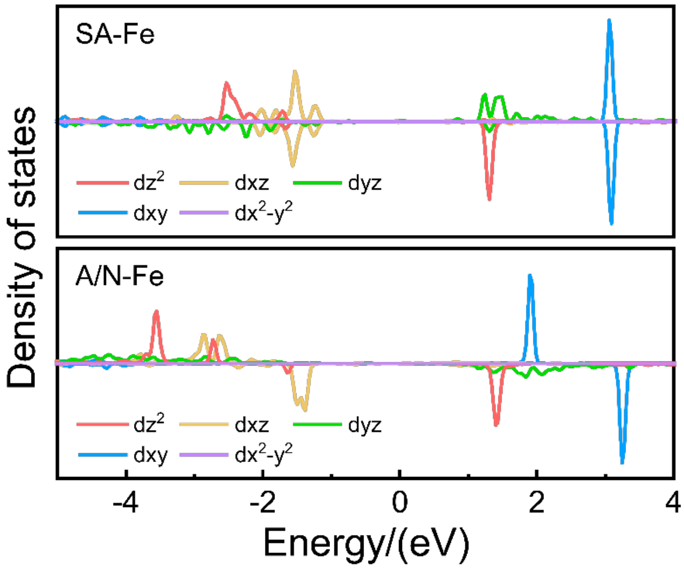

Fig. S4 Local DOS projected onto the individual *d*-orbitals of the atomic Fe site in SA-Fe and A/N-Fe. The upper and lower panels are for spin-up and -down channels, respectively. For the Fe site to adopt minimal energy mode under the built-in exchange field spreading throughout A/N-Fe, significant polarization and splitting occur on the *d*-shell. What might deserve a little more emphasis is the variation in properties of those with *z*-component (d_{xz}, d_{yz}, d_{z^2}), as the confined Fe site encounters the fact that its square planar configuration mainly spatially allows the above three having lobes lying along the vertical (*z*) axis of the carbon basal plane to interact with the adsorbate being at the atop position [13,14], which have proved to be major determinant of the catalytic activity of M–N–C toward either HER [15], or CO_2RR [16]. The exchange field alters spins and energies of these *d*-orbitals, then those of the bonded intermediates, and eventually affect the whole process of the reaction.

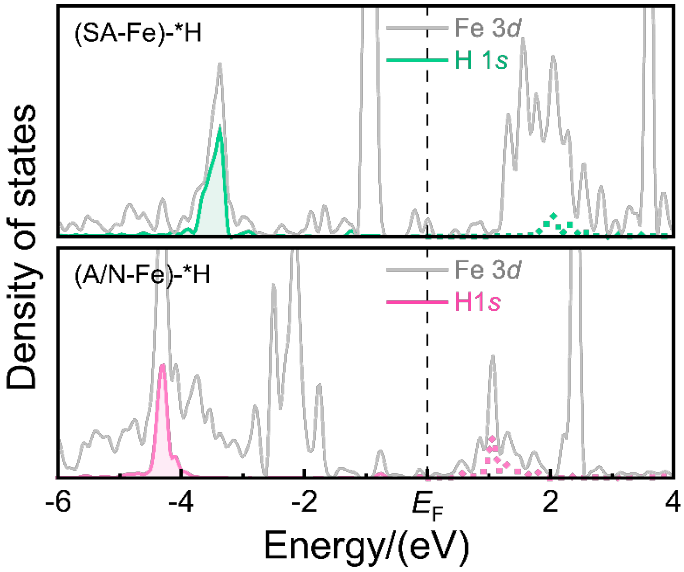

Fig. S5 Local DOS projected onto Fe 3*d* of the atomic Fe site and H 1*s* of the adsorbed H atom in (SA-Fe)-*H and (A/N-Fe)-*H.

Material Characterizations

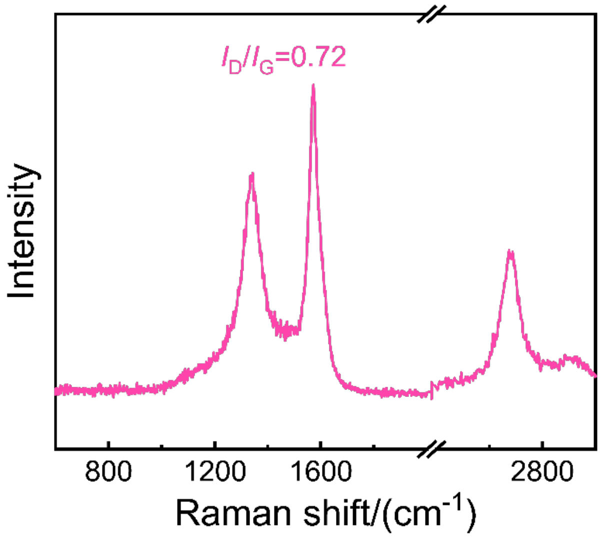

Fig. S6 Raman spectrum of Fe_3C-L@Fe-NC.

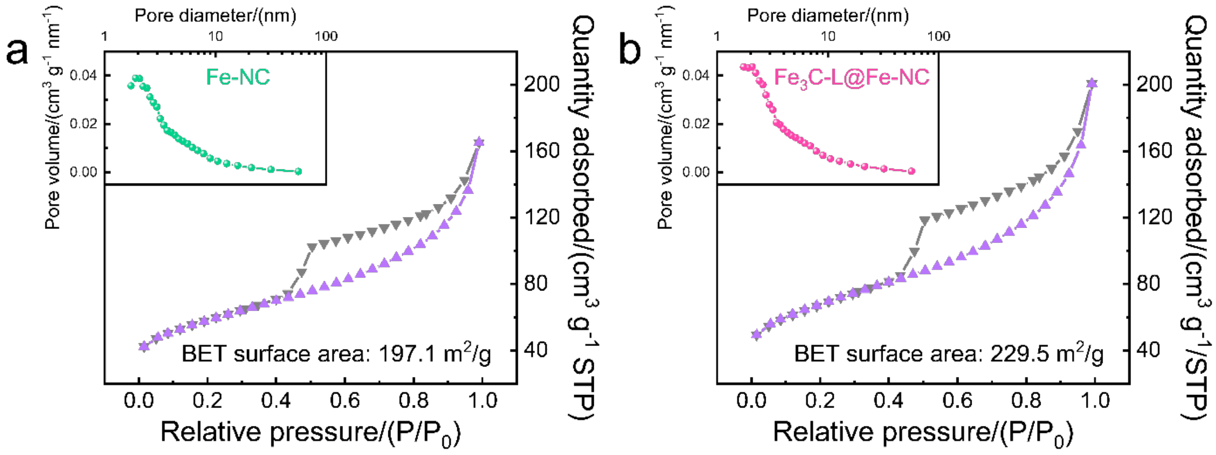

Fig. S7 N_2 adsorption/desorption isotherms and the corresponding pore size distributions of (a) Fe_3C-L@Fe-NC and (b) Fe-NC.

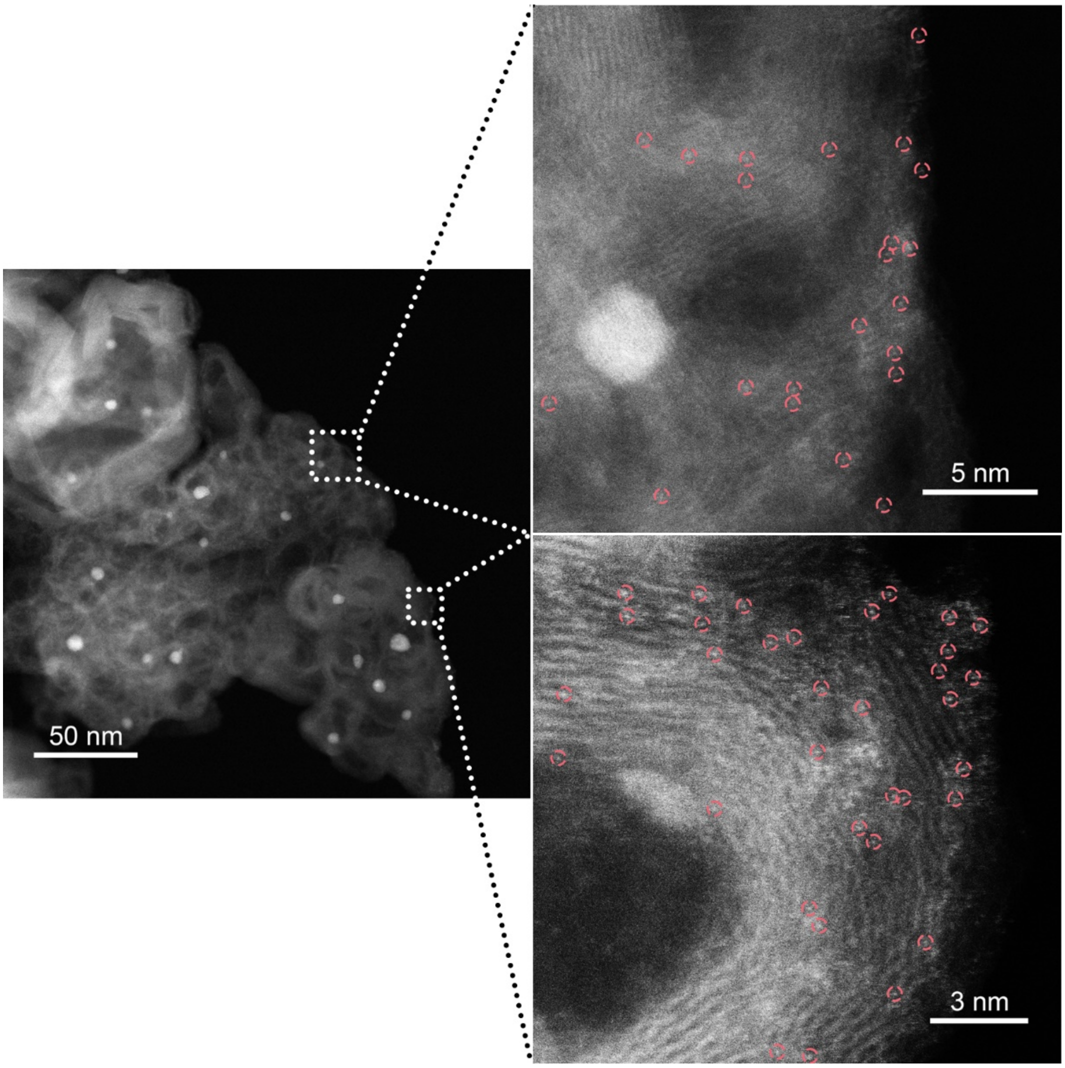

Fig. S8 AC-HAADF-STEM images of Fe_3C-L@Fe-NC.

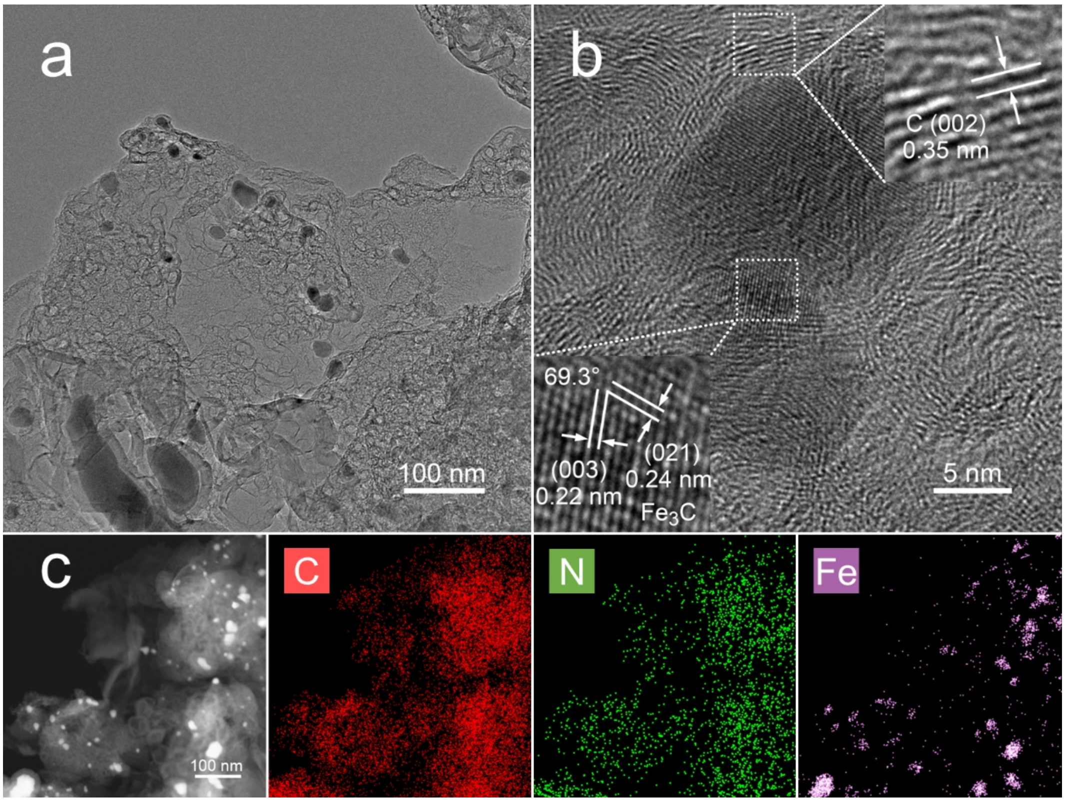

Fig. S9 (a) TEM, (b) HR-TEM, (c) STEM and EDS mapping images of Fe_3C-S@Fe-NC.

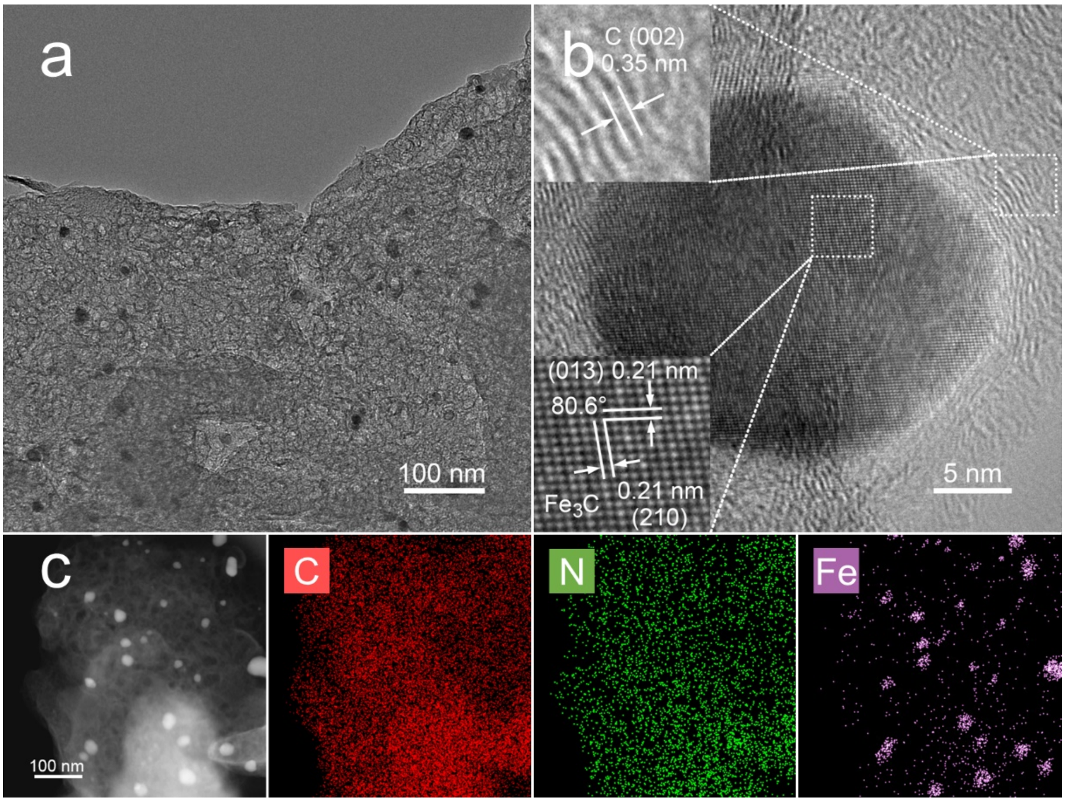

Fig. S10 (a) TEM, (b) HR-TEM, (c) STEM and EDS mapping images of Fe_3C-M@Fe-NC.

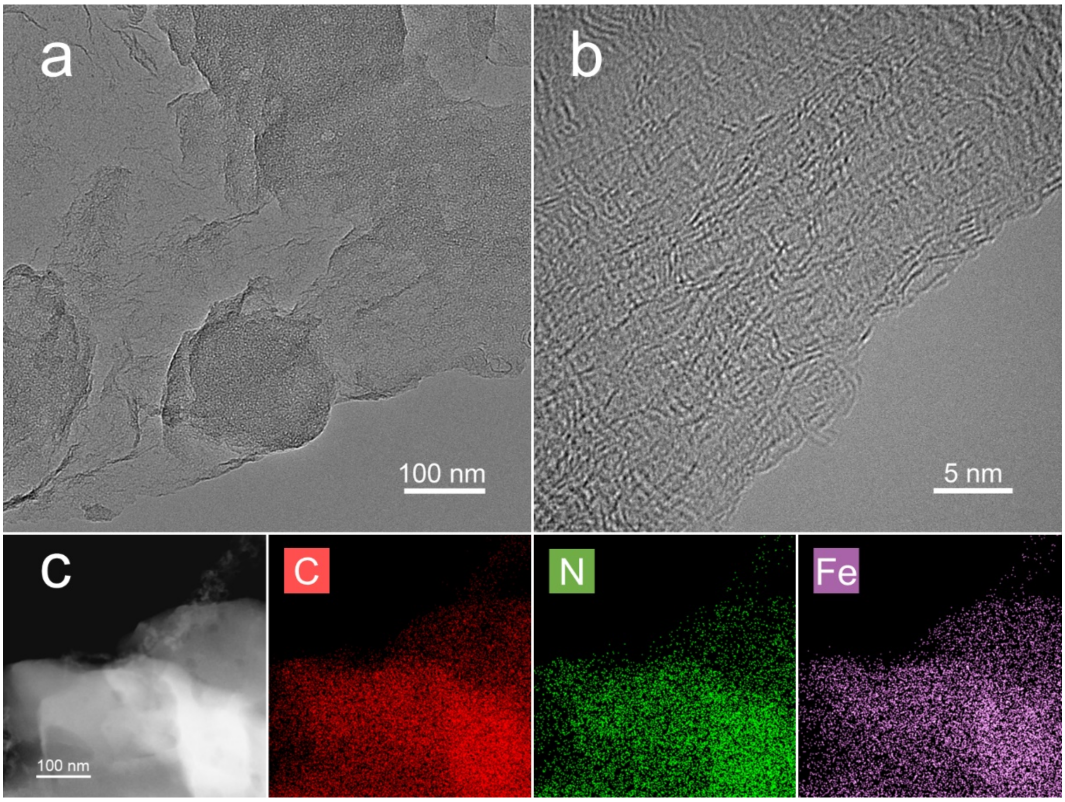

Fig. S11 (a) TEM, (b) HR-TEM, (c) STEM and EDS mapping images of Fe-NC.

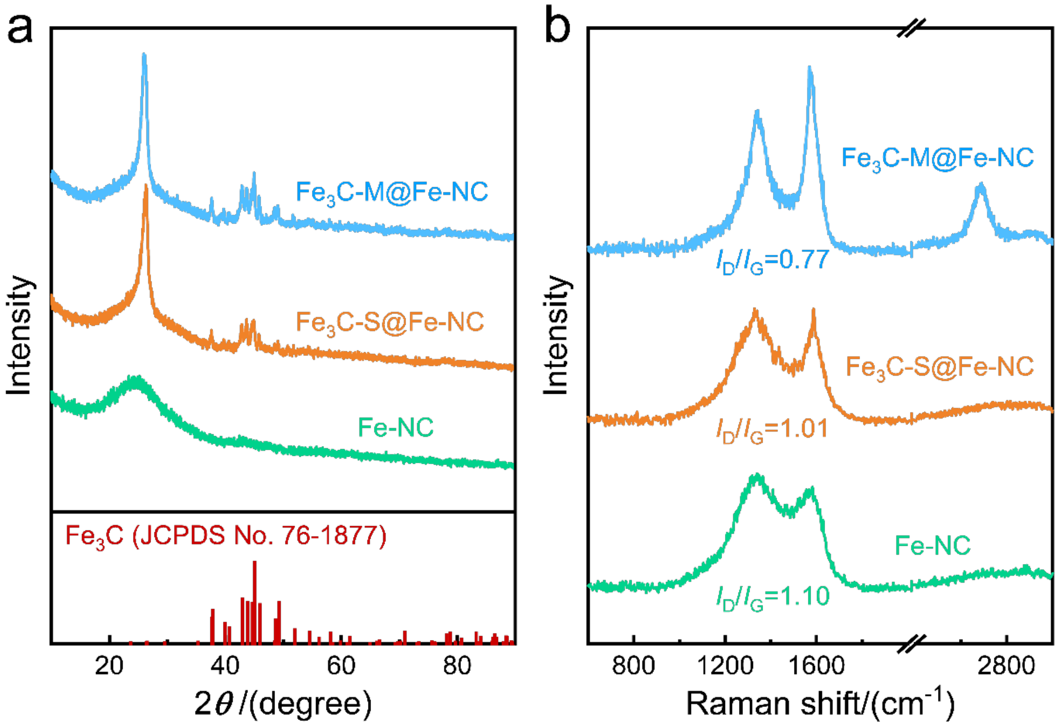

Fig. S12 (a) XRD and (b) Raman spectra of Fe-NC, Fe_3C-S@Fe-NC and Fe_3C-M@Fe-NC.

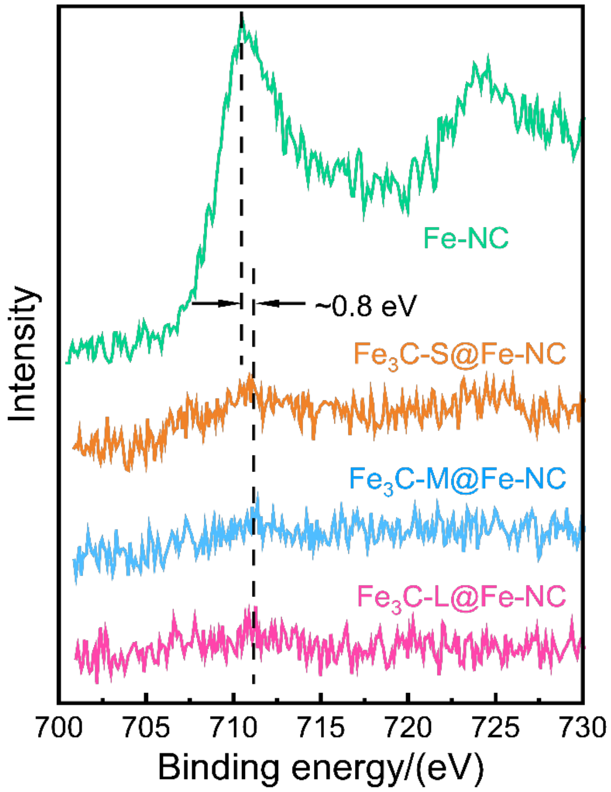

Fig. S13 XPS Fe 2p spectra of Fe-NC and Fe_3C-X@Fe-NCs. The signal around 707 eV can be assigned to Fe^0 (carbide) species, and the signal close to 710 eV matches well with the Fe configuration in Fe-N_x moiety [17–20]. Perceive that the Fe peak of Fe-N_x in Fe-NC (710.5 eV) shifts by ~0.8 eV in Fe_3C-X@Fe-NCs (711.2–711.4 eV) [17,20–22]. This phenomenon might be attributed to the interaction between atomic Fe and nanostructured Fe_3C in the A/N-Fe pairs [17,20].

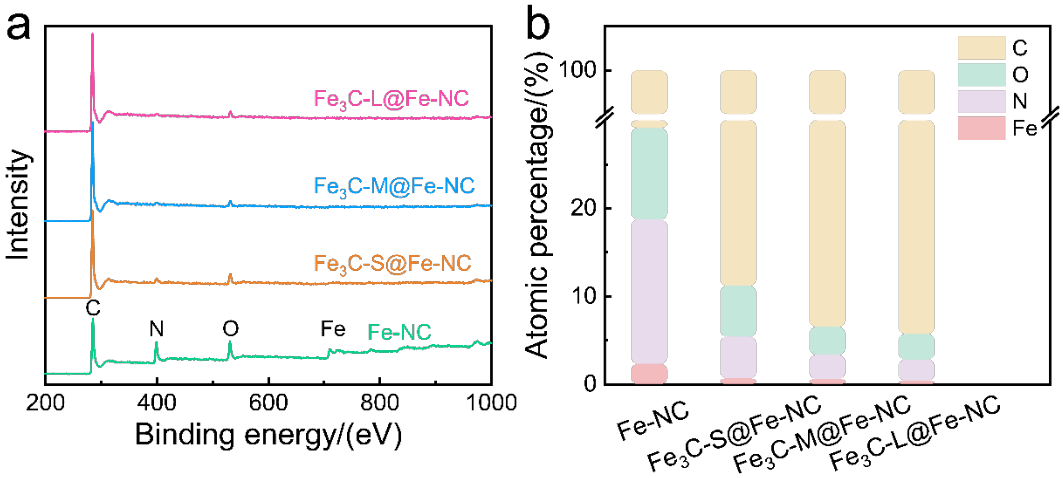

Fig. S14 (a) XPS total survey and (b) the corresponding atomic percentages (at.%) of Fe, N, O and C elements in Fe-NC and Fe_3C-X@Fe-NCs. For Fe_3C-X@Fe-NCs, since the most nanostructured Fe_3C are so encapsulated in graphitic carbon shells that could hardly be detected by surface-sensitive XPS, the share of iron reflects chiefly the proportion of atomic Fe [19,23,24].

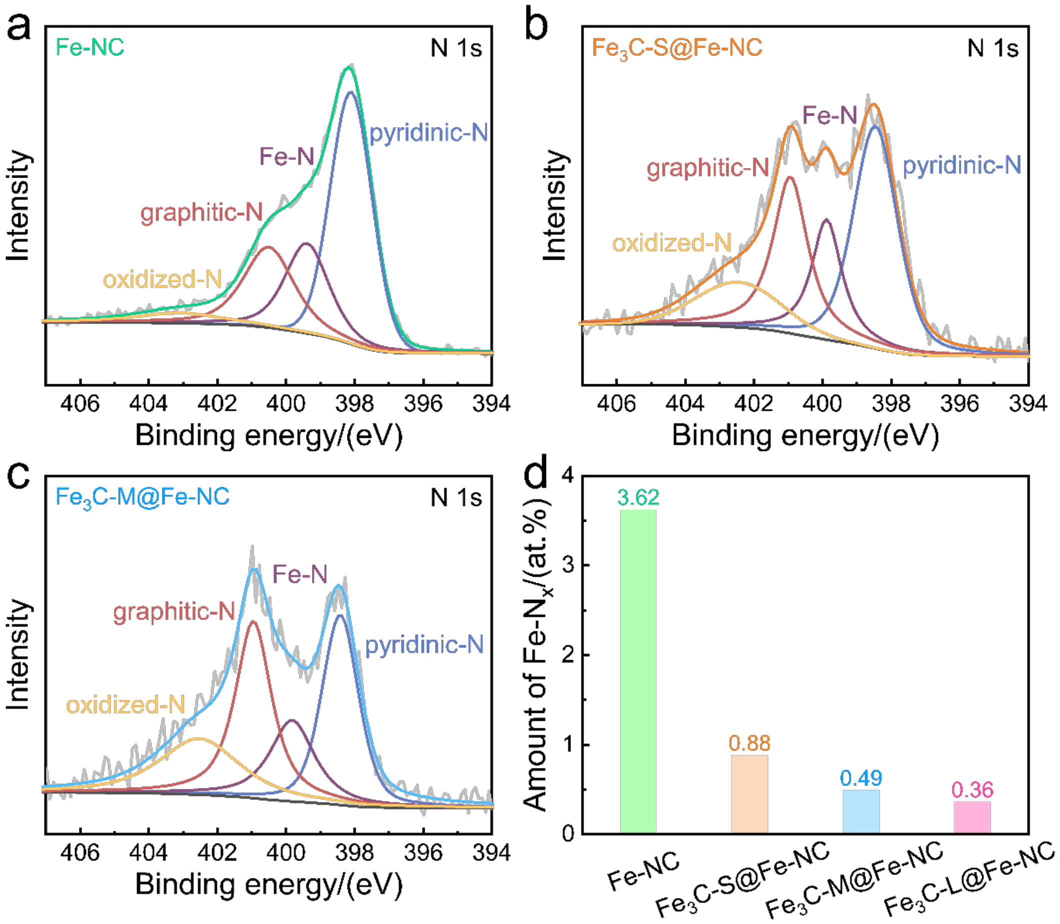

Fig. S15 XPS N 1s spectra of (a) Fe-NC, (b) Fe_3C-S@Fe-NC and (c) Fe_3C-M@Fe-NC, respectively. (d) The amounts of Fe-N component in Fe-NC and Fe_3C-X@Fe-NCs, calculated on a basis of total nitrogen content and Fe-N fraction (listed in Table S1).

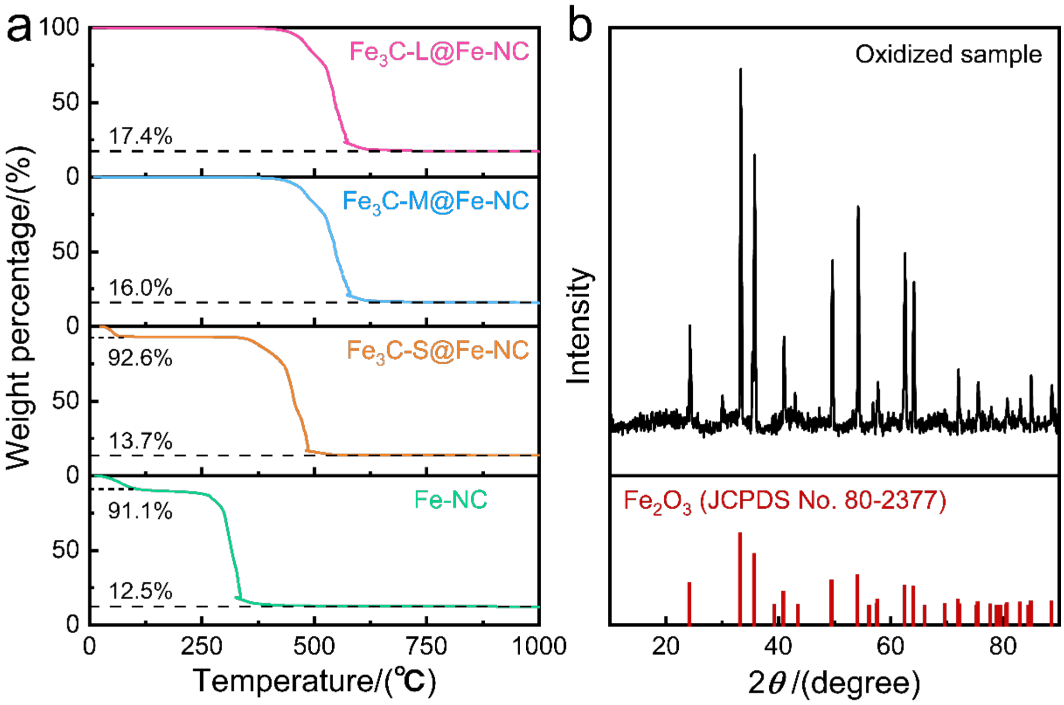

Fig. S16 (a) TG profiles of Fe-NC and Fe_3C-X@Fe-NCs, measured from room temperature to 1000 °C under air atmosphere (heating rate: 10 °C min^{-1}). Weight loss in the headspace is viewed as that from absorbed water. (b) XRD spectrum of the Fe_3C-L@Fe-NC sample after experiencing TG measurement. All the Fe species were oxidized and transformed into Fe_2O_3.

The above results exhibit a negative correlation between the two Fe species in Fe-NC and Fe_3C-X@Fe-NCs, i.e., incremental cost of isolated Fe atoms to create more condensed Fe_3C phase, which allows the A/N-Fe configuration to be adjusted accordingly.

EDS mapping images sketch the speciation of Fe element that translates from extensive dispersion in Fe-NC into local aggregation in Fe_3C-X@Fe-NCs (Fig. S9–S11). XRD spectra record the Fe_3C phase going through absent (Fe-NC), emerging (Fe_3C-S@Fe-NC), and apparent (Fe_3C-M@Fe-NC and Fe_3C-L@Fe-NC) (Fig. S12a; Fig. 1d). XPS survey spectra suggest that the content of atomic Fe gradually decreases from Fe-NC to Fe_3C-L@Fe-NC (Fig. S14b), and the amount of the N corresponding to Fe-N_x component displays a same downward trend (Fig. S15d). ICP-MS and TG data give the N_{Fe}/A_{Fe} value increasing up the series: Fe-NC < Fe_3C-S@Fe-NC < Fe_3C-M@Fe-NC < Fe_3C-L@Fe-NC (Fig. S16; Table S2).

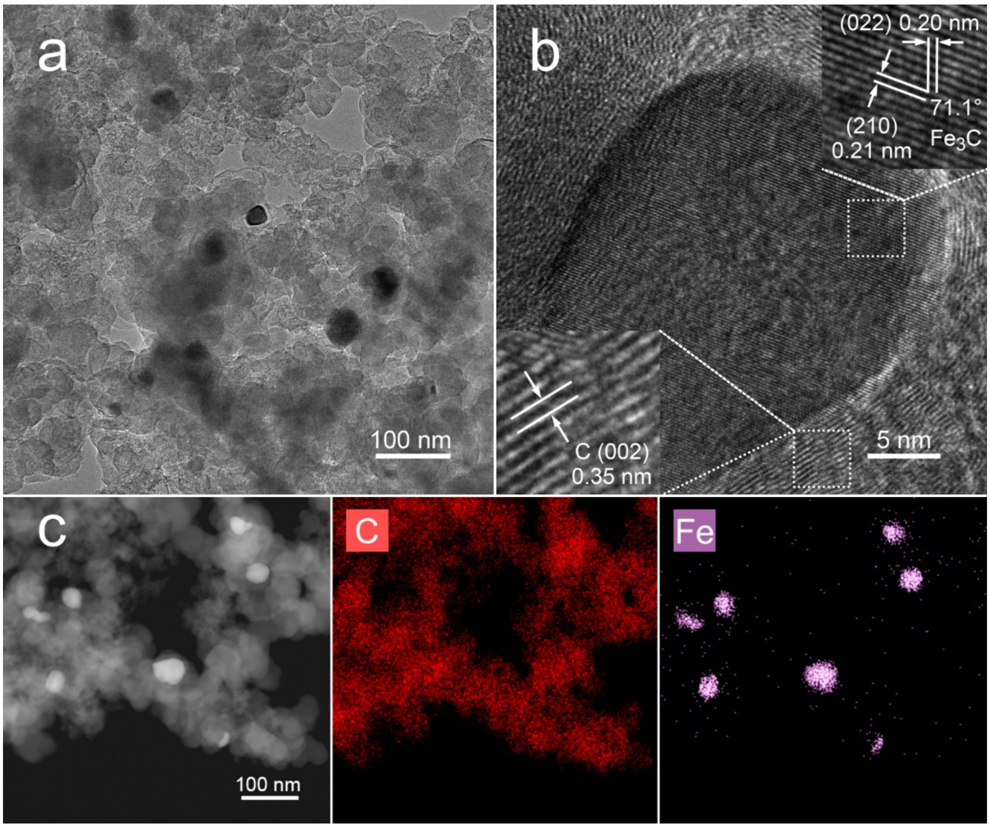

Fig. S17 (a) TEM, (b) HR-TEM, (c) STEM and EDS mapping images of FeC@C.

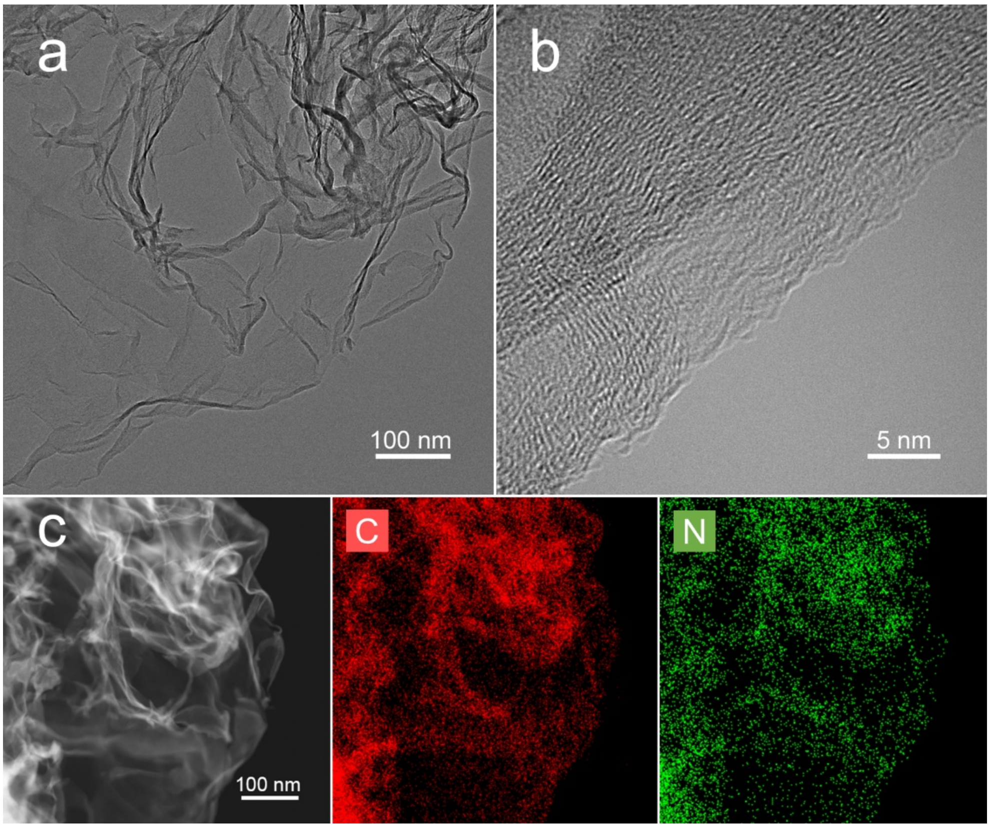

Fig. S18 (a) TEM, (b) HR-TEM, (c) STEM and EDS mapping images of NC.

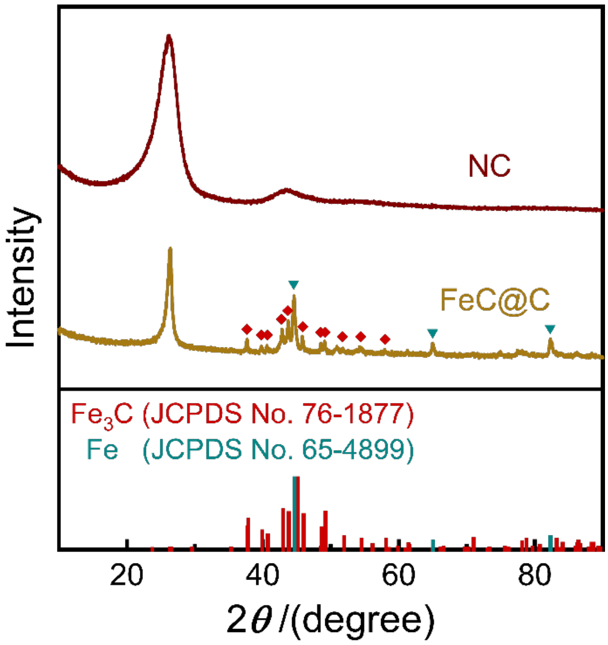

Fig. S19 XRD spectra of FeC@C and NC.

Electrochemical CO_2RR Tests

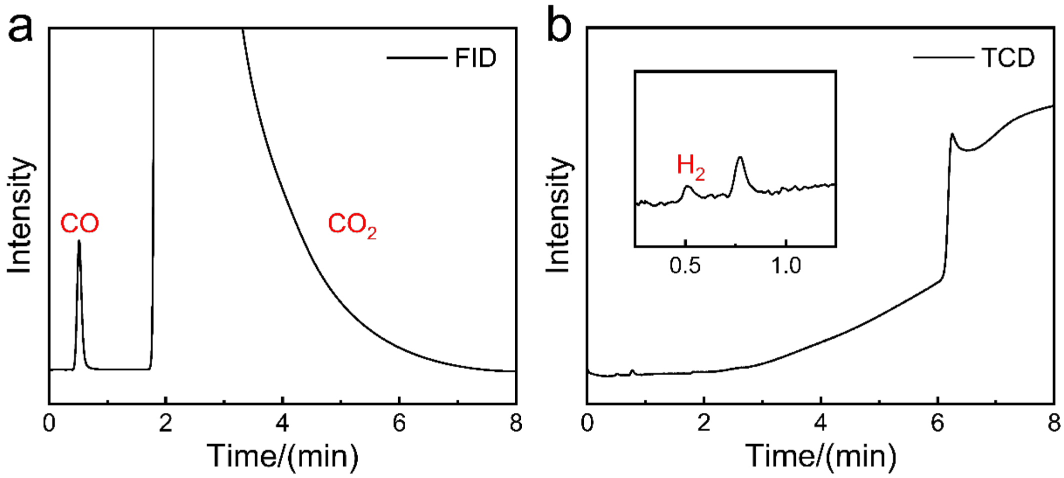

Fig. S20 GC curves for the gas products generated on Fe_3C-L@Fe-NC cathode after electrolysis at −0.40 V, recorded by (a) FID and (b) TCD detectors.

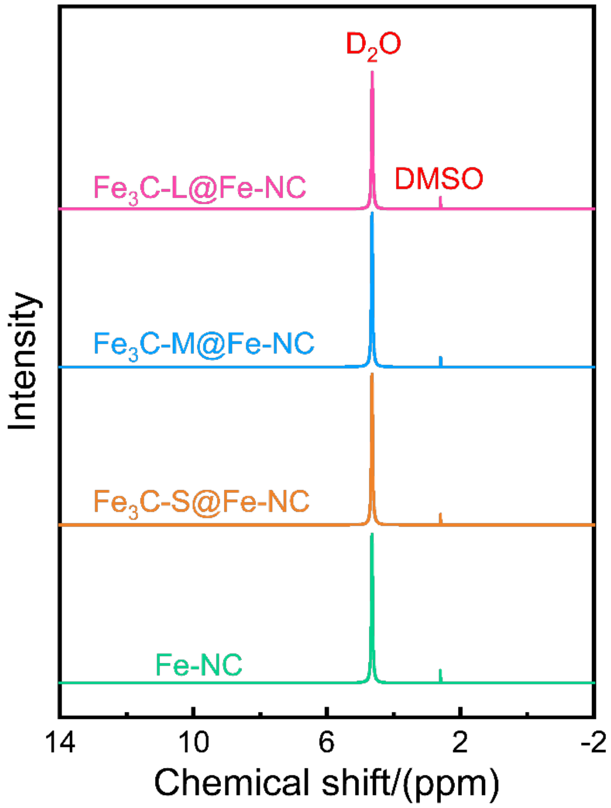

Fig. S21 ^{1}H NMR spectra of the electrolytes after constant-voltage accumulation at −0.40 V for Fe-NC and Fe_3C-X@Fe-NCs.

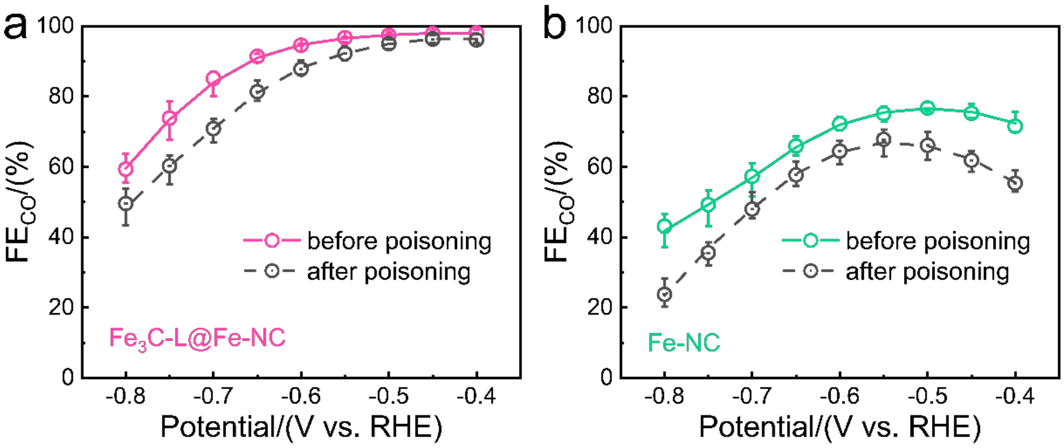

Fig. S22 KSCN poisoning experiments for (a) Fe_3C-L@Fe-NC and (b) Fe-NC. SCN^- have a strong affinity with and can thus block off the Fe-N_x sites. After poisoning, both catalysts' FE_{CO} declines dramatically, indicating that the atomic Fe centers have been deactivated in catalyzing CO_2RR.

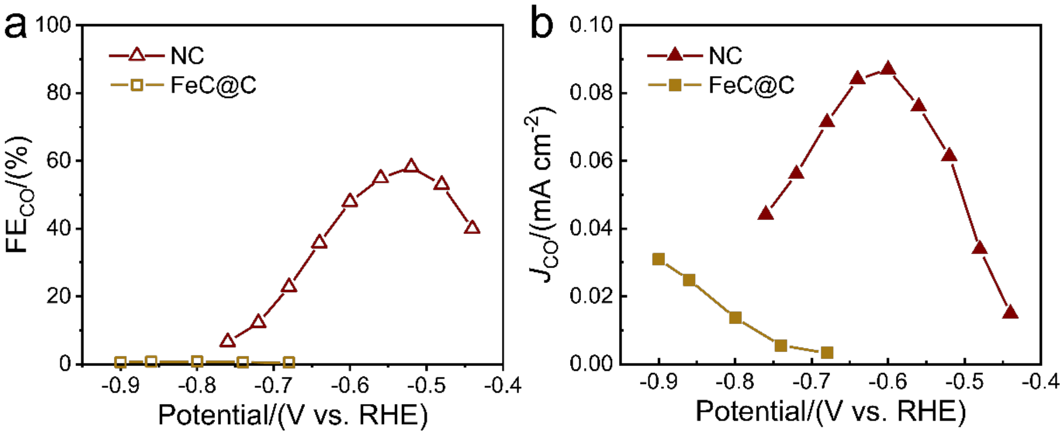

Fig. S23 (a) FE_{CO} and (b) J_{CO} of NC and FeC@C control samples.

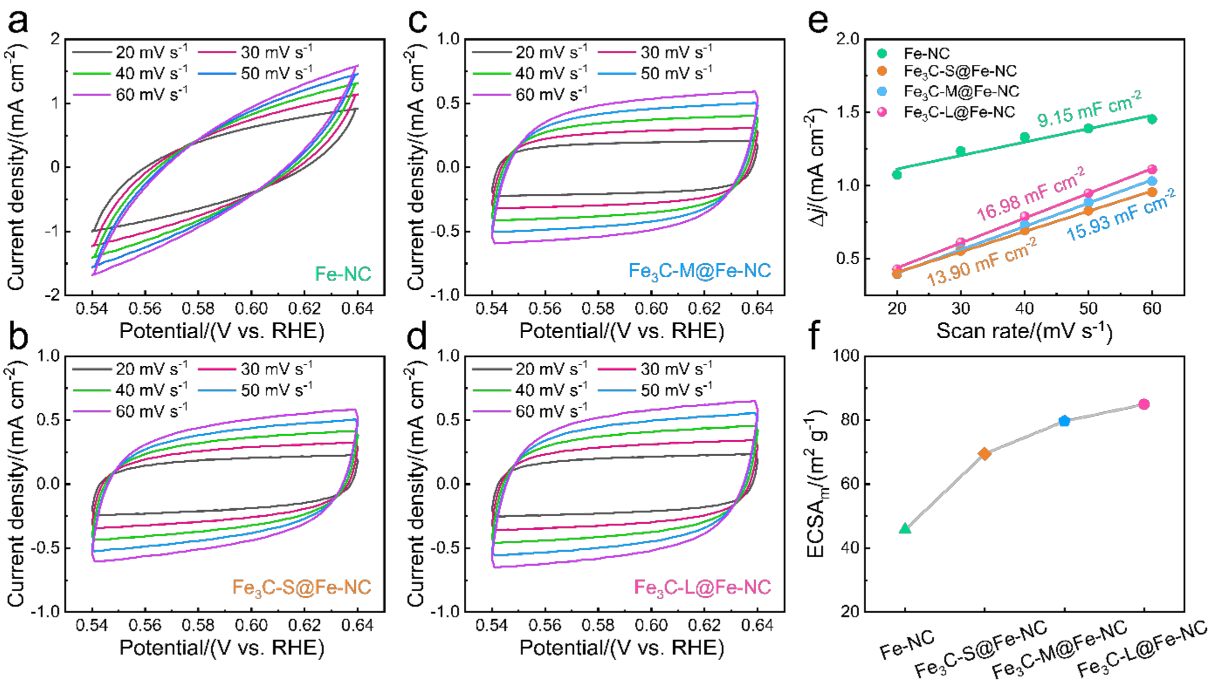

Fig. S24 CV curves collected at different scan rates for (a) Fe-NC, (b) Fe_3C-S@Fe-NC, (c) Fe_3C-M@Fe-NC and (d) Fe_3C-L@Fe-NC. (e) Linear fittings for the slope of the Δ*j* between anodic and cathodic scans vs. the scan rate to estimate the C_{dl}. (f) Mass-normalized ECSA of the above catalysts.

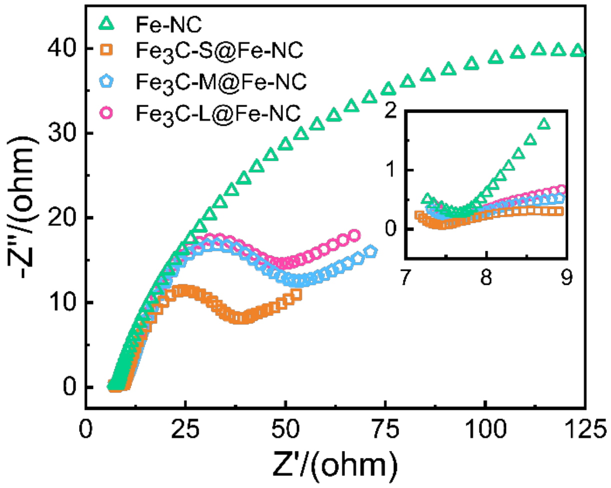

Fig. S25 Nyquist diagrams from EIS measurements for Fe-NC and Fe_3C-X@Fe-NCs.

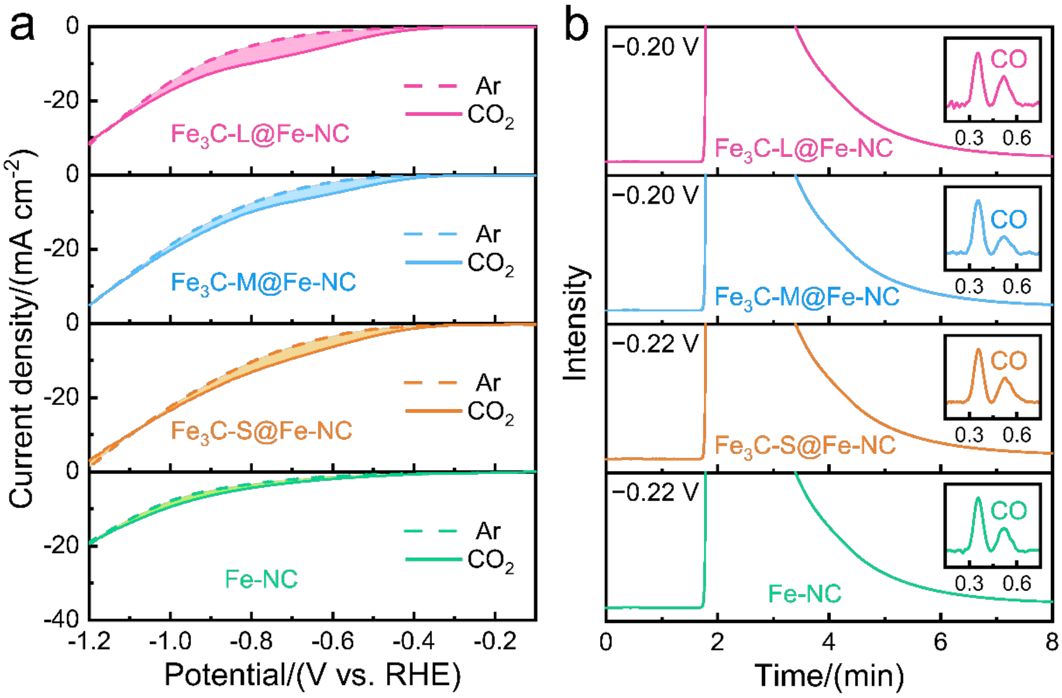

Fig. S26 (a) LSV curves of Fe-NC and Fe_3C-X@Fe-NCs in Ar- and CO_2-saturated electrolytes. The cathodic peaks are visualized by subtracting the former from the latter, and shaded in color. (b) FID curves of the gas product after the chronoamperometry for Fe-NC and Fe_3C-X@Fe-NCs, recorded at the specific potential that had been applied progressively larger until CO signal started being detectable.

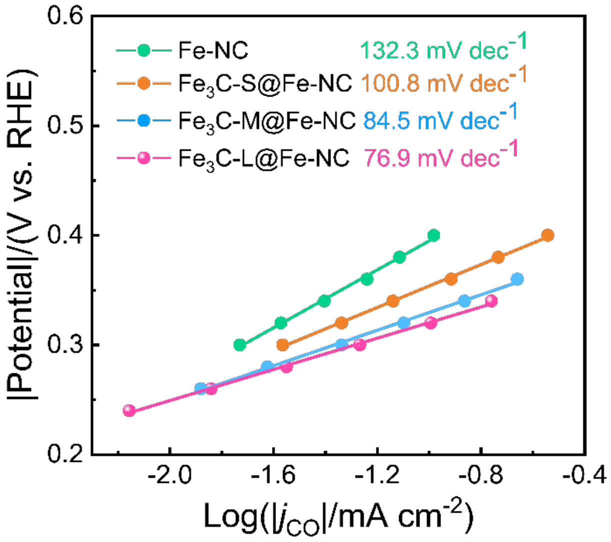

Fig. S27 CO_2RR Tafel plots of Fe-NC and Fe_3C-X@Fe-NCs. For Fe-NC with Tafel slope above 118 mV dec^{-1}, CO_2 activation is slow and limits the subsequent protonation step; for Fe_3C-X@Fe-NCs with Tafel slope below 118 and increasingly closer to 59 mV dec^{-1}, CO_2 experiences a fast 1 e$^-$ reduction to convert into $*CO_2^{\bullet -}$ awaiting being protonated [25].

Catalytic Stability

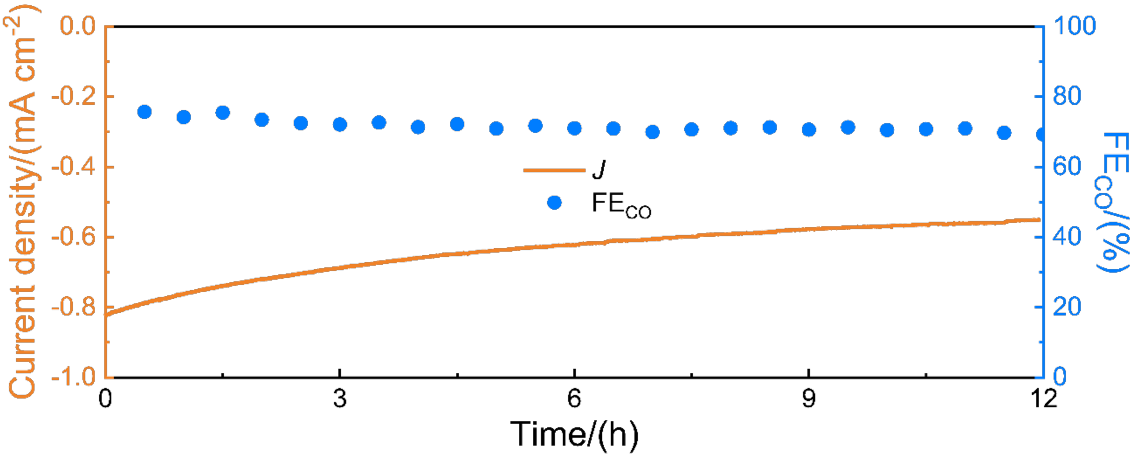

Fig. S28 Long-term chronoamperometry curve and time-dependent FE$_{CO}$ plot of Fe-NC at –0.50 V during 12 h electrolysis.

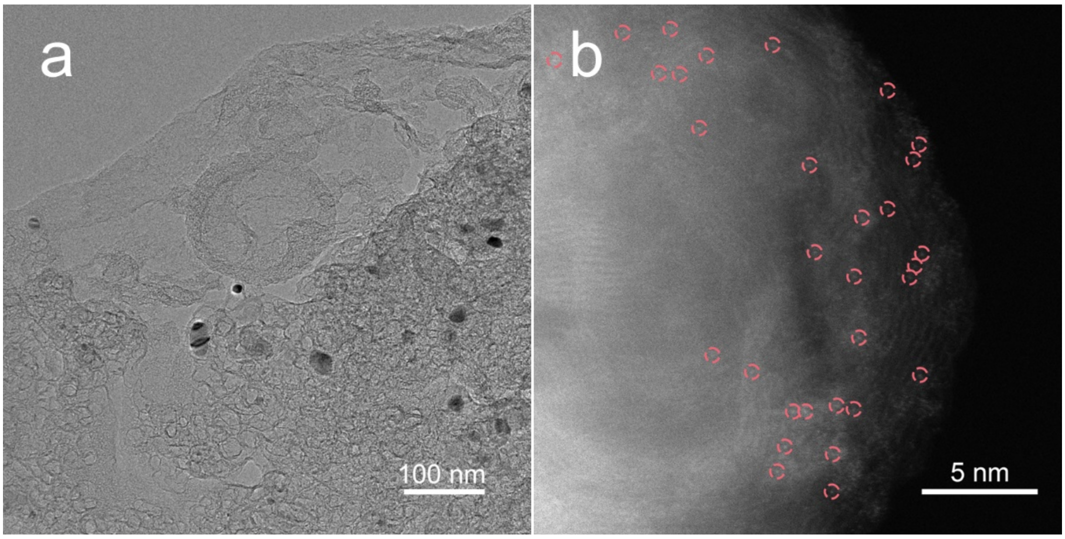

Fig. S29 (a) TEM and (b) AC-HAADF-STEM images of Fe$_3$C-L@Fe-NC after experiencing the stability test.

Flow Cell Operation

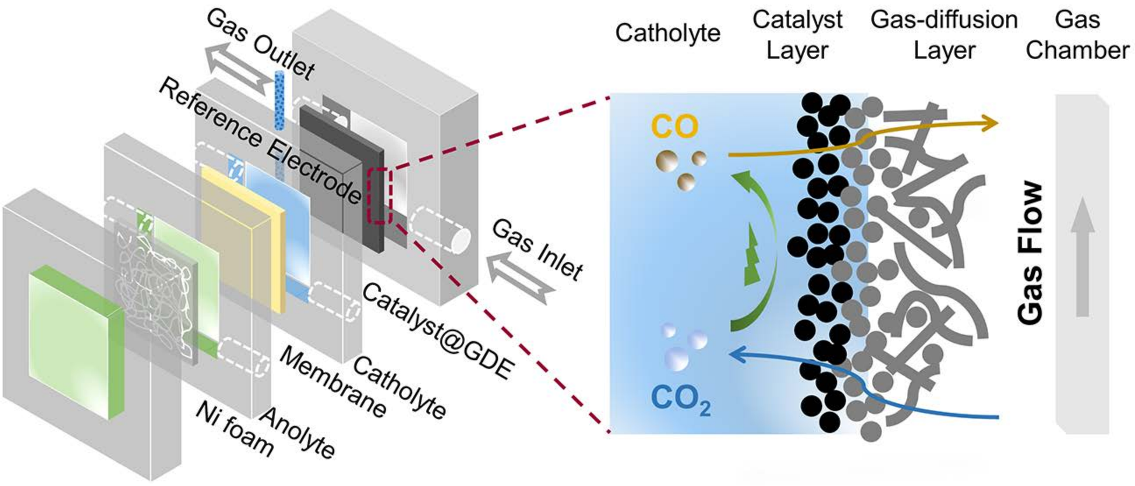

Fig. S30 Schematic of flow cell device and gas transport inside GDE for scale-up CO_2 electrolysis.

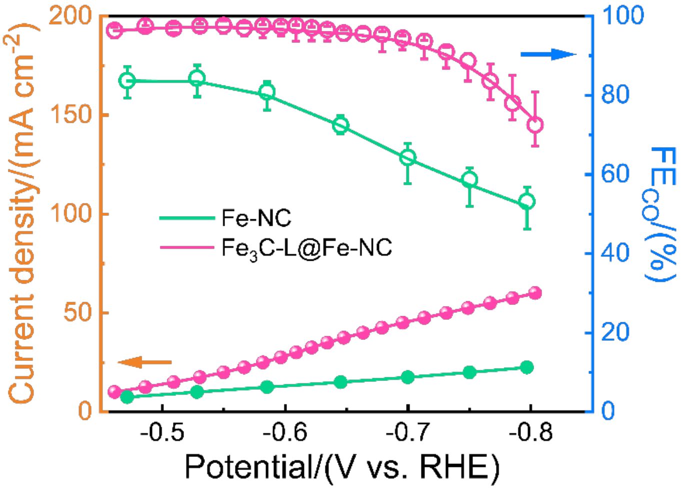

Fig. S31 Steady-state current densities and the corresponding FE_{CO} of the catalysts. For Fe_3C-L@Fe-NC, FE_{CO} > 95% can be achieved at varying constant-current points from 10 to 40 mA cm^{-2}. Maximal FE_{CO} of >97% appears at around 20 mA cm^{-2}. FE_{CO} maintains above 90% with a limiting workload of 50 mA cm^{-2}.

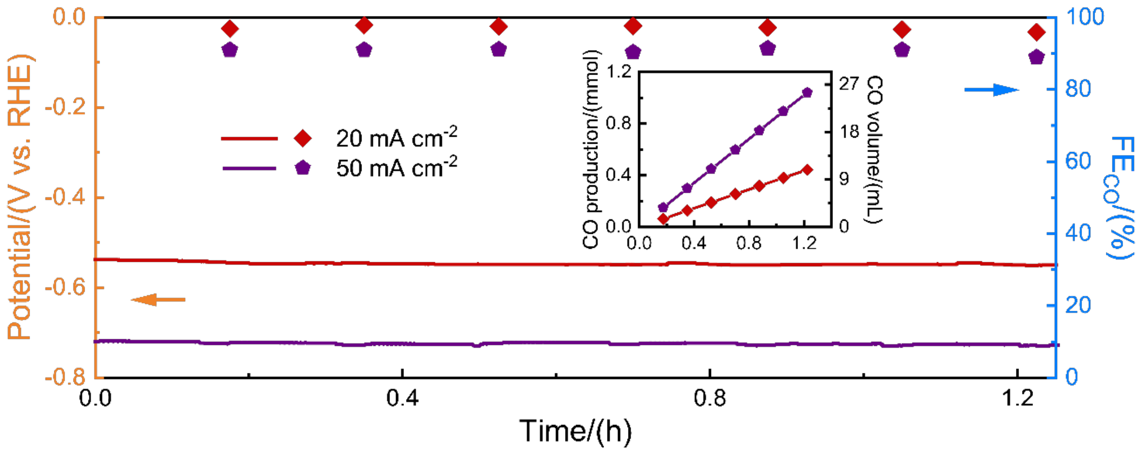

Fig. S32 Potential- and FE$_{CO}$-time responses of Fe$_3$C-L@Fe-NC operating at demonstrated current densities. Inset: accumulated CO production (moles and volume) over electrolysis time. After ~1.2 h continuous electrolysis, final CO accumulation reaches up to 1.04 mmol (25.5 mL) per cm^2 GDE.

In Situ ATR-SEIRAS Analysis

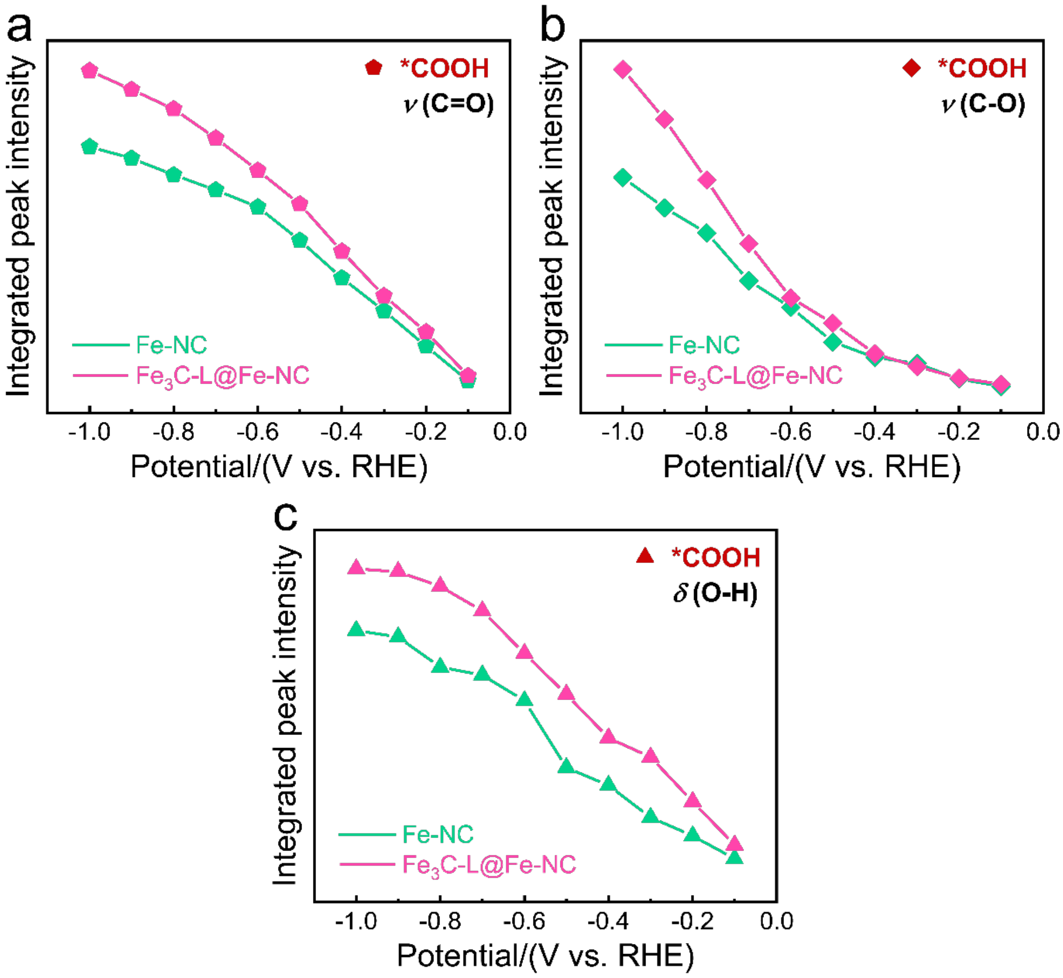

Fig. S33 Integrated intensities of *COOH-relevant vibration peaks in Fig. 3a,b: a) C=O stretch, b) C–O stretch and c) O–H deformation, as a function of applied potentials recorded during the chronopotentiometry tests. The slope (intensity vs. potential) can reflect evolution rate of the studied functional group or substance [26].

In studying a certain substance or functional group, there are both quantitative and qualitative data extracted from the spectra that answer the valuable questions about the content, as well as the structure, of this constituent, respectively. One is characteristic peak, for observation of the growth tendency. A positive peak indicates that it is produced or has increased, and conversely, with respect to a negative peak it is consumed or has disappeared. The peak intensity is directly proportional to the concentration; for accurate description, an integrated or area value is more desirable than a peak reading [27]. The other is characteristic vibration, for evaluation of the geometric strength. Remember that IR spectroscopy works by exploiting the resonance taking place when a (or part of a) molecule absorbs electromagnetic wave with frequency equal to its natural vibration. To avoid undue reconditeness, only classical, mechanical physics basis is sketched here, although a more exhaustive picture can be found in Ref. [28,29] with chapters devoted to a comprehensive account of the theory about vibrational spectroscopy.

Treat a diatomic molecule as composed of a weightless elastic spring (chemical bond) connecting the mass points (atoms). Its intrinsic motion of stretching is approximately described as a harmonic oscillation (obeying Hooke's Law) around the equilibrium. The corresponding vibrational equation is advanced by Newton's Laws of Motion, the solution of which is of the form:

$$\omega = \frac{1}{2\pi}\sqrt{\frac{k}{\mu}}$$

Where ω is the characteristic vibration frequency; μ is the reduced mass of the molecule; k is the restoring force constant, defined by the sum of all forces that act between the atoms.

Owing to the atomic scale involved, this model should be broadened to quantum mechanics. That is, the energy uptake ΔE for the system to jump from a ground to an excited vibrational level is quantized:

$$\Delta E_{\omega} = h\omega\Delta \mathrm{v}$$

Where h is Planck's constant; v is the vibrational quantum number. According to Selection Rule, here only the transition of $\Delta\mathrm{v}=1$ is allowed.

Radiation energy E_v and frequency v of the electromagnetic wave follow the relationship:

$$E_v = hv$$

To realize the resonance excitation, frequency principle must be fulfilled:

$$E_v = \Delta E_\omega$$

Thus

$$\nu = \frac{1}{2\pi}\sqrt{\frac{k}{\mu}}\ \Delta \mathrm{v}$$

Where k is, clearly, positively correlated with ν. An evident descriptor of k—magnitude of the interaction along the internuclear axis—is bond length, reflective of the binding strength. This immediately draws a conclusion: for the same bond geometry, the shorter the length (larger k), the higher the frequency (ν), and vice versa.

The above criterion automatically holds true for any component unit (bond, group, etc.) in a certain polyatomic system, because a characteristic mode could actually involve significant motions of only the relevant atoms—approach to the treatment of them resembles that just presented—constituting a discrete unit, and hence have a frequency primarily determined by the nature of this unit itself.

Rechargeable Zn–CO_2 Battery Performances

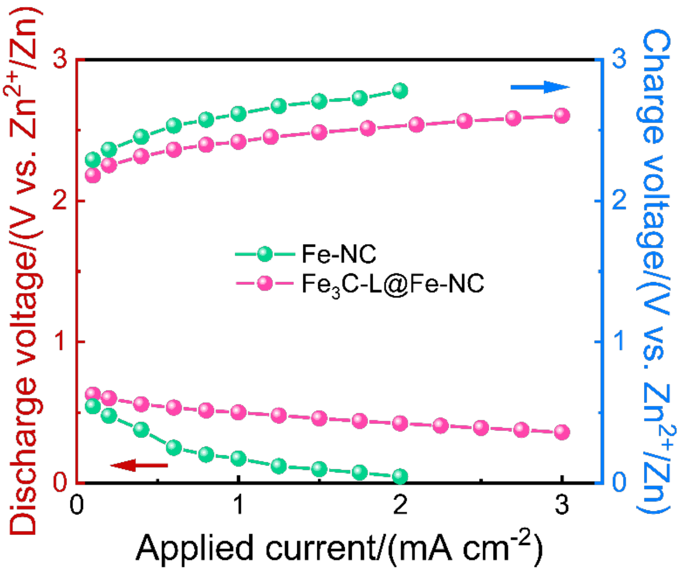

Fig. S34 Discharge and charge voltage plateaus at varying constant currents of Fe_3C-L@Fe-NC– and Fe-NC–equipped ZCBs.

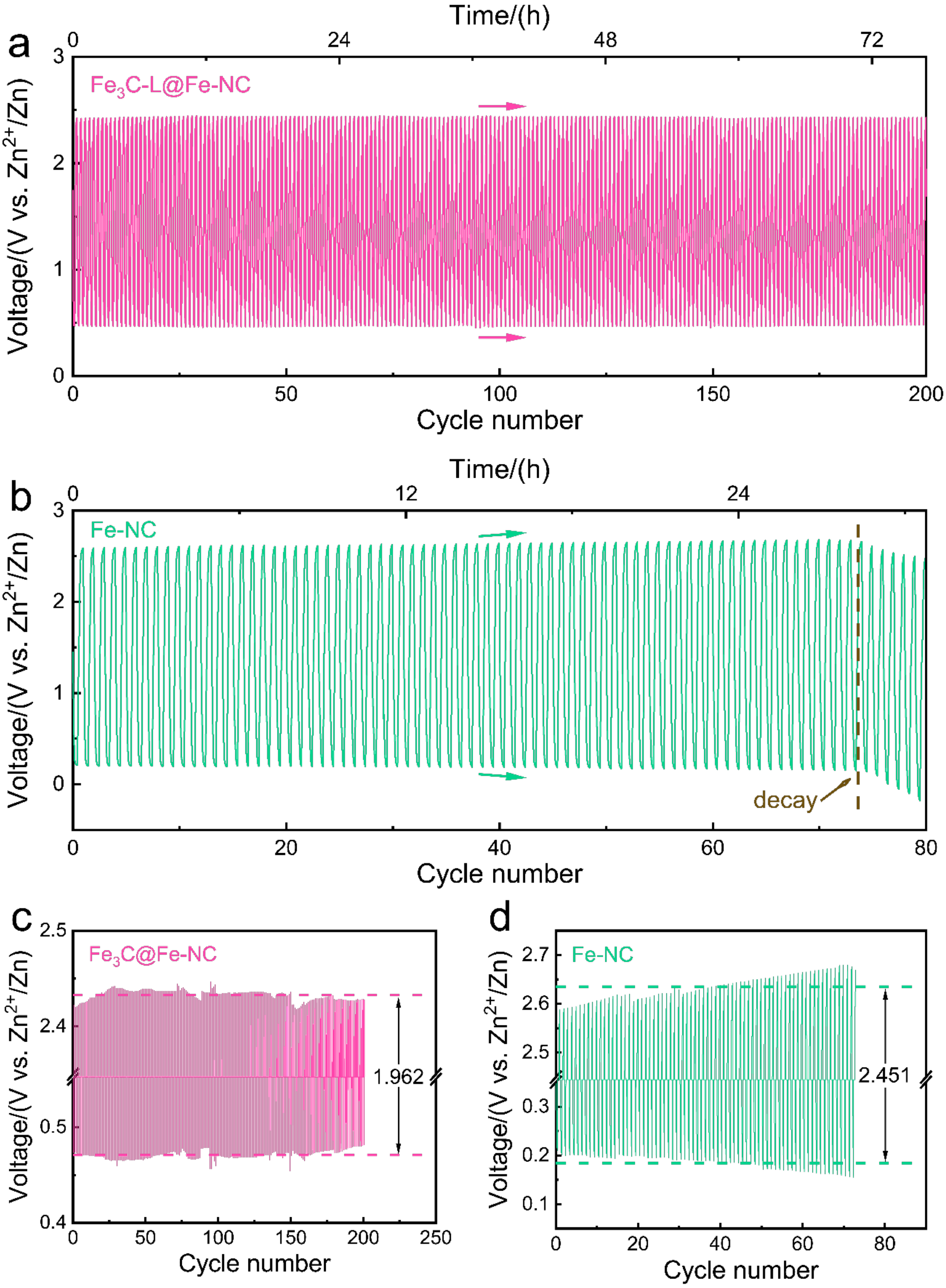

Fig. S35 Galvanostatic discharge/charge cycling curves at 1.0 mA cm^{-2} and the corresponding average charge-discharge voltage gaps. (a,c) 200 cycles and (b,d) 80 cycles for Fe$_3$C-L@Fe-NC– and Fe-NC–equipped ZCB, respectively.

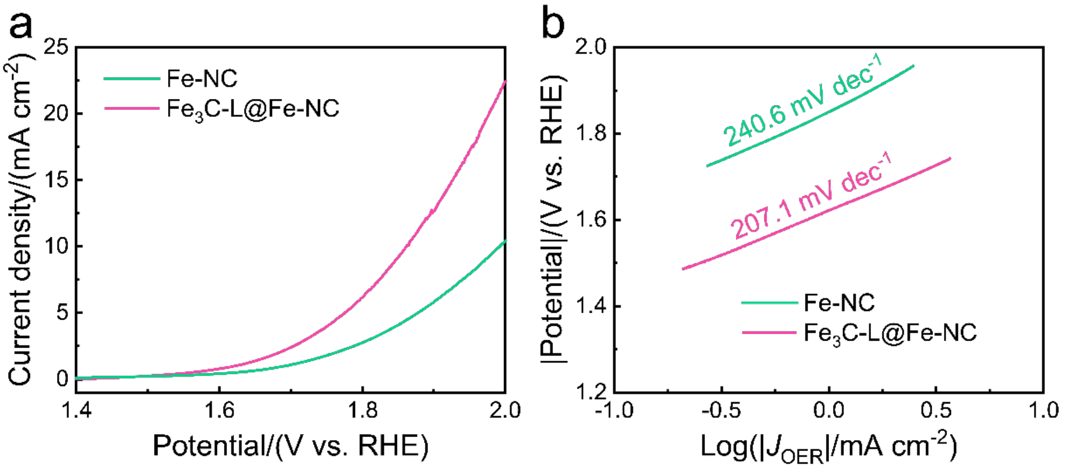

Fig. S36 (a) OER LSV curves and (b) OER Tafel plots of Fe-NC and Fe_3C-L@Fe-NC.

In an ideal rechargeable ZCB (no parasitic HER occurs), the cell reactions are as follows [30]:

During discharge process, CO_2RR occurs on the cathode propelled by anodic Zn dissolution:

Cathode: $CO_2 + 2H^+ + 2e^- \rightarrow CO + H_2O$

Anode: $Zn \rightarrow Zn^{2+} + 2e^-$

$$Zn^{2+} + 4OH^- \rightarrow Zn(OH)_4^{2-}$$

Overall discharge reaction:

$$Zn + CO_2 + H_2O + 2OH^- \rightarrow Zn(OH)_4^{2-} + CO$$

During charge process, cathodic OER occurs to reduce Zn^{2+} to be deposited on the anode:

Cathode: $H_2O \rightarrow 1/2O_2 + 2H^+ + 2e^-$

Anode: $Zn(OH)_4^{2-} \rightarrow Zn^{2+} + 4OH^-$

$$Zn^{2+} + 2e^- \rightarrow Zn$$

Overall charge reaction:

$$Zn(OH)_4^{2-} \rightarrow Zn + 1/2O_2 + H_2O + 2OH^-$$

Schemes

Transport Chain of Spin Polarization from Nanostructured Fe_3C to Atomic Fe

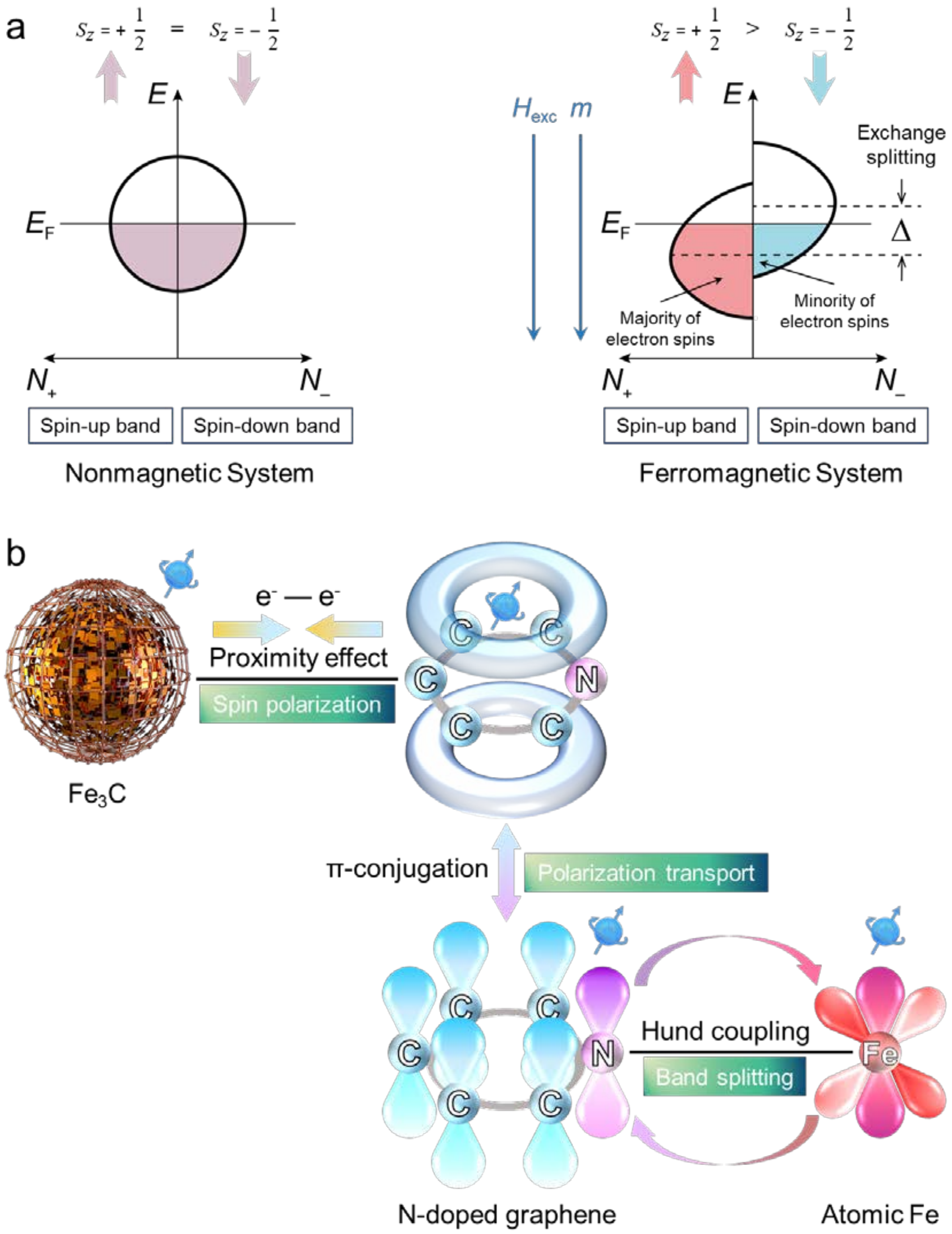

Scheme S1 (a) Band models of nonmagnetic (left) and ferromagnetic (right) transition metals, illustrated for the *d*-shell. DOS is approximated by a simple semicircle; filled electron states below the Fermi surface E_F are marked in shadow, hole states above the E_F blank. In nonmagnetic situation, electrons occupy a level with two opposite spins, exhibiting an equilibrium population of spin-up and spin-down states with no net spin. In ferromagnetic situation, define a quantization direction, typically labelled *z*, then "up" along *z* and "down" along -*z*. For the sake of discussion, take -z as the direction of an exchange field H_{exc}, used to align the magnetization moment m in the system. So m is also in the down direction. Because the moment m and spin s have opposite signs ($m = -g\mu_B s$), spin-up and spin-down should be majority and minority states, respectively. The center of spin-up band downshifts and that of spin-down uplifts, giving an energy separation—the exchange splitting Δ. (b) Transport chain of the spin polarization in Fe_3C-X@Fe-NC system. The lobe of each orbital that has positive phase is dark-colored, and the negative lobe light-colored. The blue up-arrows denote not the realistic spin of a certain electron, but the sign of net spin by summing over all states (i.e., the direction of spin polarization) on each building unit. The interactions (at the interfaces between the units) that stabilize and conduct the polarization are labelled by gradient-color double-headed arrows. The terminal point, atomic Fe center, receives a duplicated band splitting along an orientation similar to that of the starting point, Fe_3C, via this chain.

For condensed ferromagnetic Fe_3C, *exchange interaction* builds (strictly speaking, can be treated as) an internal magnetic field superposed on the electrons inside the lattice [31,32]. Under this *exchange field*, *d*-band divides into two sub-bands, each of which comprises states with spin up or down: the spins (up) with orientation anti-parallel to the field are subjected to lower "magnetic potential energy", and the parallel ones (down) higher. To minimize total energy of the system, electrons tend to adopt codirectional arrangement—they repel each other—by occupying the levels separately rather than doubly occupy an individual level with opposite spins (in the latter case, one of the two electrons would be inevitably parallel to the field direction) [33,34]. This criterion perforce drives a relative displacement between spin-up and spin-down, termed *exchange splitting* and illustrated pictorially in Scheme S1a, which, explicitly, spreads the bottom of the former toward low-energy side away from E_F to vacate the *d*-levels as much as possible for a larger population of electrons prone to set themselves at up spin—from the viewpoint of electrons over the entire *d*-shell, they are thereby *spin-polarized* [12,35–37]. The Fe_3C DOS with asymmetrical spin channels (see the dark-red line in Fig. S3a) intuitively depicts the dominant filling of spin-up as against its counterpart [38].

Intentional adhesion to magnetic particle as a spintronic building block can also polarize the spin states of graphene that forms a resultant long-range ferromagnetic ordering via *proximity effect* [12,39–44], originating from the exchange interaction (non-zero overlap integral between the wavefunctions of the local moments in Fe_3C and of the itinerant electrons in graphene) [39,40] within the charge transfer region at the interface of Fe_3C/graphene junction (see Fig. S2a) [45–47]. Since the microscopic law of exchange interaction dictates that the minimum energy mode happens only when an electron flitting from one atom to the neighbor takes the same orientation as that of the electrons in both atoms [48,49], namely, this electron inherits the sign of net spin already existing in the previous unit and will pass it on to the next when being exchanged, C p_z electrons (π-band) undergo proximity-induced exchange splitting preferably along the identical polarization direction as the incorporated Fe_3C [50–52]. This effect, then, benefiting from excellent charge and spin mobilities of the graphene, is transmitted a sizable distance through carbon basal plane [53,54], finally to reach the anchored Fe-N_x moieties.

Analogous to the case of the carbonaceous macrocycle fence in transition metal complexes [55], the π-band of the surrounding graphitic layers, as part of the coordination shell, tailors greatly the d-states of the metal center [56,57]. To be specific, mediated by the intervening N ligands that donate their p_z orbitals to π-conjugation on the honeycomb skeleton and simultaneously p-d π-bonding of the N-Fe coordination [58], there is an expected quasi-hybridization (indirect mutual overlap) between cyclic C p_z orbitals and central Fe d orbitals (especially those with z-component (d_{xz}, d_{yz}, d_{z^2}) due to the close symmetry matching), in which general Hund's Rule operates to align the spin polarization of both orbital sets with each other [59], and ultimately "inject" the exchange splitting into the Fe center.

Now, a transport chain of spin polarization is granted permission to run throughout the entire A/N-Fe system (Scheme S1b). Exchange interaction provides the required spin alignment to preserve the original spin information of Fe_3C before and after the polarization crosses the chain links (i.e., Fe_3C/graphene interface and C-N-Fe bridge), which is what underlies the proof that the DOS of Fe–N–C begins mirroring the asymmetric shape characteristic of Fe_3C (Fig. S3a). A splitting picture is thus painted on the electronic structure of the atomic Fe site; in a manner akin to that invoked for the polarization source—Fe_3C (Scheme S1a), it broadens the d-band and downshifts the d-band center.

Antibonding π* Molecular Orbitals and Descriptor of Protonation Difficulty

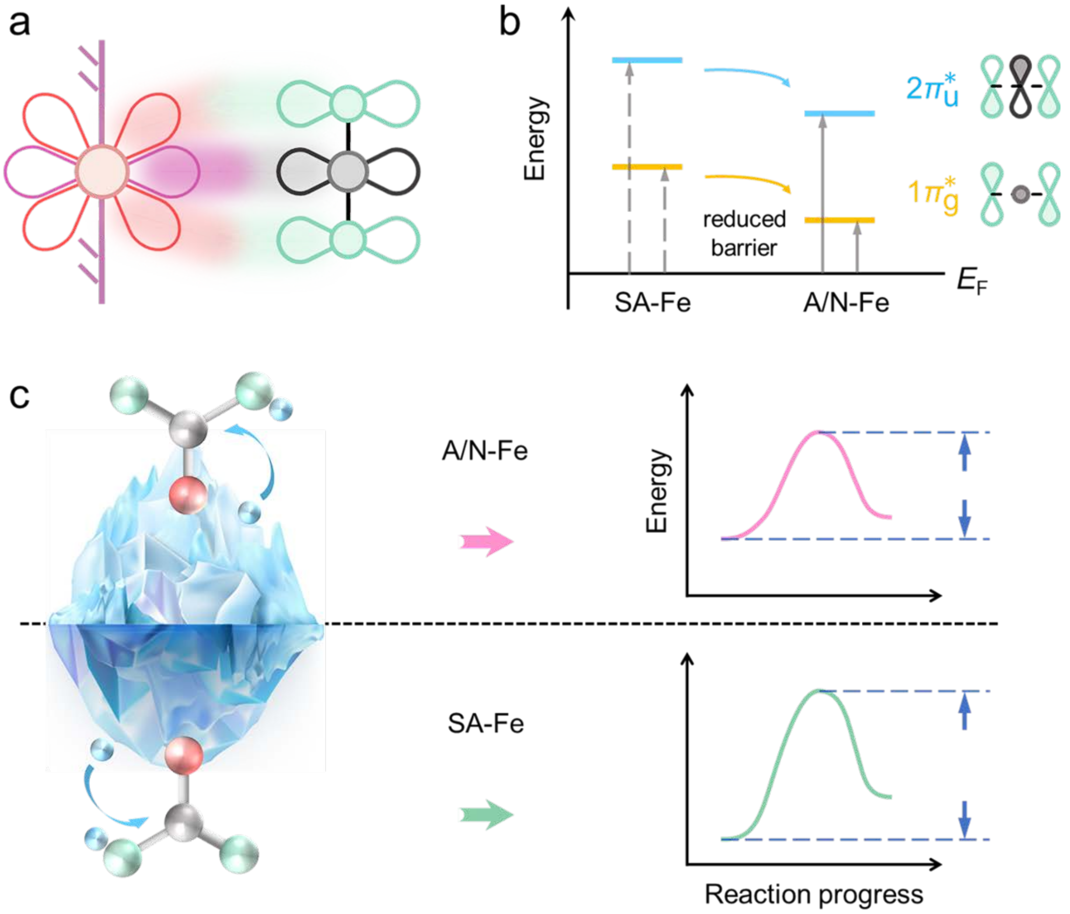

Scheme S2 (a) Schematic illustration of the coupling between the atomic Fe's *d* orbitals and a CO_2-derived intermediate's π-type molecular orbitals. (b) Schematic comparison of transition barriers of the electron to be filled into the antibonding molecular orbitals of the COOH outside SA-Fe and A/N-Fe. H atom is omitted. The right-hand side draws contour representations of the $1\pi_g^*$ and $2\pi_u^*$ frontier orbitals. Spatial distribution of the C 2*p* and O 2*p* are defined by black and blue contours, respectively. Colored shading means positive phase in the wavefunction, and blank shading means negative. Nodal planes are formed by the mutually orthogonal phases. The dashed lines connecting the atoms signify that population of these two orbitals will be conducive to cancel the binding forces between C and O. (c) Putative free energy diagrams for the protonation steps over SA-Fe and A/N-Fe.

Before embarking on a qualitative, versatile descriptor of the difficulty of protons' attacking on CO_2-derived species, some approximations to be made for molecular orbital (MO) energy-level diagram (that draws the electronic structure) of the intermediates would help simplify the problem, in view of the following arguments. The discussion begins with a representative key intermediate, *COOH, and can be conveniently extended to include the others.

The core idea is to divide the *COOH into two units relatively independent of each other. First, the bare H ion linked to the terminal O atom of the adsorbed CO_2 does not change inherent number of CO_2 MOs' nodal planes (that arranges the MOs' energy sequence) [60,61] lying between the C and each O. Secondly, electrons entering the empty H 1*s* orbital all come from the σ lone pairs present in pure CO_2 2σ MOs [62,63]; the former can roughly be viewed as just a dispensable satellite of the latter in the CO_2–H mixing. Thirdly, since this $CO_2 \rightarrow H^+$ electron donation is σ-type (along the connection line of O–C–O), its perturbation on the π-type MOs (perpendicular to the O–C–O line) is even more diluted. Consequently, it can reasonably be assumed that combination with H^+ to form *COOH will be to modify, but not drastically distort, both energy sequence of and energy difference between the MOs of original CO_2 molecule. Hence, for simplicity, the O–H covalency is neglected and the MO diagram of *COOH is regarded as an approximate equivalent to that of its CO_2 parent. One can invoke the group of rules and parameters—label (designation), symmetry, ordering, etc.—established for defining the MOs in CO_2 to describe their counterparts in *COOH, especially the most important two: $1\pi_g^*$, the highest occupied molecular orbital (HOMO), and $2\pi_u^*$, the lowest unoccupied molecular orbital (LUMO) [62,63].

The behavior of a molecule bound to a metal center can be treated as a simple two-level scenario that resembles the constructive or destructive overlapping of two sets of atomic orbitals (AOs) to produce deep-lying bonding or high-lying antibonding MOs [64–66], only in which one set has been replaced by the molecule frontier orbitals (the HOMO and LUMO, main members responsible for molecule-metal interaction) [67,68] and the other the metal *d*-band center (the average over all of the *d*-states). This picture is further proved correct by the fact that, here in the case of CO_2RR proceeding on M–N–C system, the TM-COOH adduct (TM = e.g., Mn, Fe, Co, Ni) preferentially adopts η^1(C) configuration (i.e., as shown in Fig. S2b, the bottom of the central C atom is fixed to the TM along the latter's *z* axis, with the two O atoms hanging at left and right sides of the C) [16], whereby only π-type MOs of the *COOH—exactly its frontier orbitals ($1\pi_g^*$ or $2\pi_u^*$)—are symmetry-adapted to be hybridized with the TM *d*-orbitals (Scheme S2a) [58,69]. Then the HOMO/LUMO is split into one bonding and one antibonding contribution with energy levels below and above its initial position, respectively. Even so, each of the contributions is still part of the wavefunction of, and thus inherits the nature from [70,71], the $1\pi_g^*$ or $2\pi_u^*$—both are also, noteworthily, the *COOH's own antibonding orbitals [62,63]—implicated. That is, electron population in these new parts reflects in essence that in the old *COOH antibonding orbitals [67,68]. As the population becomes greater, binding forces within *COOH that maintains the geometry is gradually counteracted—the Pauli repulsion (internuclear distance) between C and O atoms becomes increasingly stronger (longer) [66,72,73]; accordingly, the C–O bond would gain more chances to be broken when sustaining the constant battering from protons. Considering the levels of the bonding part commonly far below the Fermi level (E_F) and fully filled, the position of those of the (empty) antibonding part (denoted E_{π^*}) relative to the E_F is of particular interest [74,75]. Antibonding electron population of the *COOH depends on the magnitude of this energy difference (denoted ($E_{\pi^*} - E_F$)), which can be used to describe the difficulty of protons' attacking the O atom off: the smaller the ($E_{\pi^*} - E_F$), the larger the population, the easier the oxygen loss.

Fig. 1f shows the local DOS projected on C & O 2*p* orbitals of the *COOH after coupling with *d*-orbitals of the atomic Fe site. The vast majority of the states above the E_F is assigned to the antibonding part derived from the *COOH frontier orbitals, which possesses prominent C–O π^* features—orthogonal (i.e., zero-integral) overlapping of the C and O 2*p* orbitals. Compared with SA-Fe, DOS peaks of the reshaped antibonding orbitals of the *COOH outside A/N-Fe move down toward and get closer to the E_F, i.e., decreased ($E_{\pi^*} - E_F$). This phenomenon has two origins. One is the downshift of the Fe *d*-band center. It brings the E_{π^*} into obtaining, as dictated by the energy perturbation equation deduced from MO theory [76], a less energy gain and an associated relative downshift (it would not be pushed upward too much when being produced). The other is the proximity-induced magnetic ordering in the Fe center (mechanism regarding this point has been outlined in Scheme S1). Under principle of spin angular momentum conservation, migration of the carriers from the Fe center (that has already been polarized by Fe_3C) to the adsorbed *COOH is also spin-polarized [43,44]. This spin-selected electron exchange between site and intermediate during electrocatalytic process would polarize the latter's spin [77,78]; concomitantly, its *p*-levels together with, of course, the MOs that the *p*-levels have produced, undergo exchange splitting that makes them descend in energy (Scheme S1a). As a result, external electrons are allowed to transfer to the C–O π^* MOs more smoothly (Scheme S2b), reducing kinetic barrier for the C–O bond dissociation and thus the second protonation step *COOH → *CO + H_2O (Scheme S2c) [79–81].

The physical picture presented above automatically hold true for $^*CO_2^{\bullet-}$ that resembles CO_2 even more strongly. It may be safely predicted that A/N-Fe can, working in a similar fashion, pull the antibonding MOs of $^*CO_2^{\bullet-}$ downward to the E_F, weaken the C=O bond for easier O accepting H^+, and dynamically boost the first protonation step ($^*CO_2^{\bullet-} \rightarrow$ *COOH) as well.

Electron Transfer Barriers in Different Fe–N–C Systems

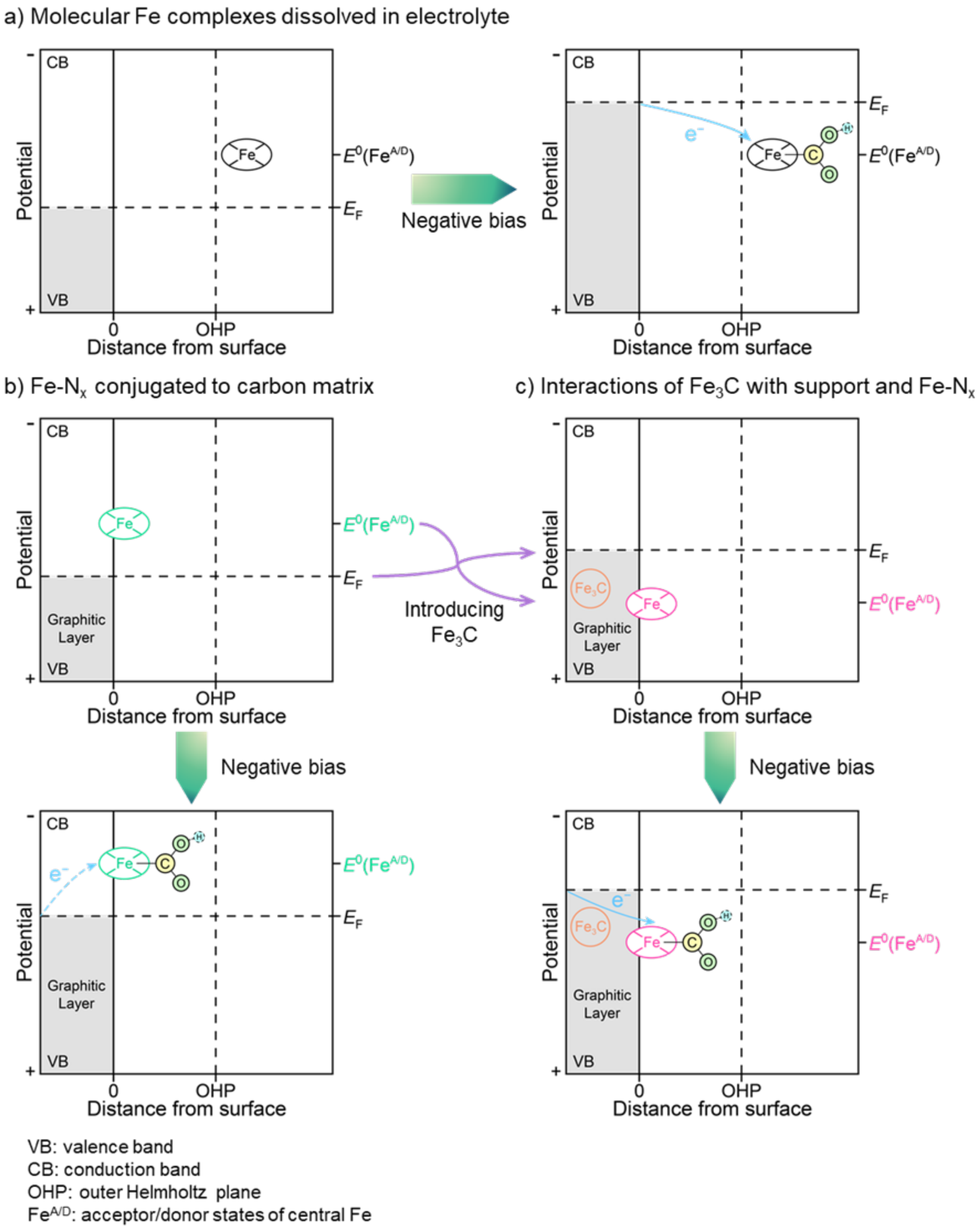
a) Molecular Fe complexes dissolved in electrolyte

b) Fe-N_x conjugated to carbon matrix

c) Interactions of Fe_3C with support and Fe-N_x

Scheme S3 Putative interfacial free energy diagrams for electrodes with (a) hypothetical Fe macrocyclic analogues, (b) single-atom Fe site anchored on graphitic carbon, and (c) A/N-Fe pair anchored on graphitic carbon. Scenario B and C correspond to Fe-NC and Fe_3C-X@Fe-NC, respectively. Each diagram displays the changes in position of Fermi level of the electrode (E_F) and redox potential of the central Fe (E^0), upon varying the voltage bias. Driving force of electron transfer (ET) is determined by the difference between E_F and E^0.

For the dissolved molecular complexes (scenario A), active species are separate from the electrode, so ET proceeds via an outer-sphere mechanism, wherein electrons tunnel across the solvent at the interface then to the external active sites. Since electrode potential only affects the E_F via charge build-up near the electrode surface—not the E^0 that still remains constant, ET driving force is potential-sensitive and adjustable [82,83]. For the Fe-N_x moieties in conjugation with graphitic carbon matrix (scenario B and C), quite the contrary, the metallic properties of graphite entail an inner-sphere mechanism, wherein reactant ions/molecules that cross the double layer are accompanied by a coincident ET traveling through the internal aromatic and heteroatomic orbitals to the active sites. Upon application of a potential, the strong coupling of the Fe centers to the highly conductive matrix guarantees that the ensuing interfacial charge build-up would raise E_F and E^0 synchronously by a similar magnitude, i.e., the initial offset of E_F relative to E^0 remains nearly unchanged [83–85]. In this case, ET driving force is, to a large extent, invariant to the applied potential but dependent on the inherent distribution of energy states within the conjugated system—fortunately, the latter can be altered by extra functional modification.

Based on calculational and experimental results, incorporation of nanostructured Fe_3C (N_{Fe}) would impose electronic perturbation on two key modules of the Fe–N–C system: uplift the E_F at graphitic electrode by activating the surrounding carbon layers (N_{Fe}-graphite interaction) [11,21,23], and downshift the E^0 of acceptor/donor states by inducing a higher valence in the isolated atomic Fe (A_{Fe}) centers (N_{Fe}-A_{Fe} interaction) [17,20]. Hypothesize that these interactions are powerful enough to shift E_F and E^0 along their respective, predetermined orientations (as just presented) by such a considerable degree that enables to close the gap between or even to invert the relative level of E_F vs. E^0. Unlike the upward climb for ET, presumably, in the pristine Fe-NC, this new energy pattern might facilitate a waterfall-like charge flowing down from the carbon matrix to the Fe sites, which accelerates tremendously the progress of electron-consuming steps including $CO_2 \rightarrow {}^*CO_2^{\bullet -}$ and $^*COOH \rightarrow {}^*CO$, providing another solid foundation for faster proton utilization.

Proton Utilization over SA-Fe during CO_2RR

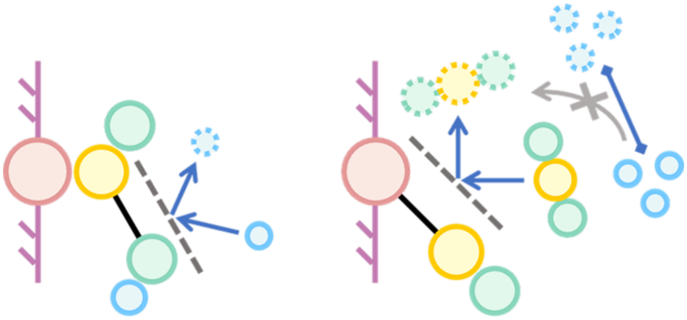

(SA-Fe)−*COOH (SA-Fe)−*CO

Scheme S4 Proposed causes of the poor proton utilization over the intermediates outside SA-Fe (red ball: Fe atom; yellow: C; green: O; blue: H). During the second protonation step (left), the rigid C–O bond resists attack from the protons that would therefore not be successfully consumed. During the CO desorption step (right), the tight Fe–CO bonding blocks the stream of protons to CO_2RR, since there is, obviously, seldom adequate amount of newly bonded CO_2 standing ready to accept them. Excessive accumulation of the unreacted protons here could be one of the potential hazards leading to (they have nowhere else to go, apart from) the unpleasing HER.

Tables

Table S1 Nitrogen contents and the deconvoluted N 1s peaks in Fe-NC and Fe_3C-X@Fe-NCs, fitted from XPS data.

Catalysts	Total N (at.%)	Pyridinic N		Fe-N_x		Graphitic N		Oxidized N	
		Position (eV)	Fraction (%)	Position (eV)	Fraction (%)	Position (eV)	Fraction (%)	Position (eV)	Fraction (%)
Fe-NC	16.41	398.1	48.84	399.39	22.09	400.5	23.26	403.08	5.81
Fe_3C-S@Fe-NC	4.73	398.46	40.2	399.88	18.56	400.94	27.49	402.45	13.75
Fe_3C-M@Fe-NC	2.74	398.42	29.33	399.82	17.87	400.95	31.47	402.53	21.33
Fe_3C-L@Fe-NC	2.27	398.5	28.17	399.66	15.77	401.18	43.66	402.87	12.4

Table S2 Iron compositions of Fe-NC and Fe_3C-X@Fe-NCs, quantified by TG, XPS and ICP-MS.

Catalysts	Total Fe (wt.%)	Atomic Fe (A_{Fe}, wt.%)		Nanostructured Fe_3C (N_{Fe}, wt.%)	N_{Fe}/A_{Fe} ratio
	TG	XPS	ICP-MS	TG−ICP-MS	
Fe-NC	9.60	8.95	9.21	/	/
Fe_3C-S@Fe-NC	10.35	4.58	5.07	5.28	1.04
Fe_3C-M@Fe-NC	11.22	2.76	2.38	8.84	3.71
Fe_3C-L@Fe-NC	12.21	1.81	1.89	10.32	5.46

Table S3 Comparison of CO_2RR performance between Fe_3C-L@Fe-NC and other reported non-precious TM/N–co-doped carbon-based SACs with maximal FE_{CO} > 90% [1,25,86–96].

Catalysts	Maximum FE_{CO} (%)	Overpotential (mV)	Potential window for FE_{CO} > 90% (V)	Tafel slope (mV dec^{-1})	Ref.
Fe_3C-L@Fe-NC	98	290	−0.34 ~ −0.64 (0.3)	76.9	This work
Co-N_5/HNPCS	99.4	680	−0.57 ~ −0.88 (0.31)	/	[86]
FeN_5	97	350	−0.46 (/)	/	[1]
(Cl, N)-Mn/G	97	490	−0.5 ~ −0.7 (0.2)	/	[87]
A-Ni-NSG	97	610	−0.72 ~ −1.12 (0.4)	114	[88]
Ni-N_3-NCNFs	96.6	590	−0.7 ~ −0.8 (0.1)	71	[89]
Fe_1NC/S_1-1000	96	390	−0.4 ~ −0.6 (0.2)	96.5	[90]
Ni-N-Gr	95.1	590	−0.7 ~ −0.9 (0.2)	126	[91]
ZnN_x/C	95	320	−0.43 ~ −0.53 (0.1)	167	[92]
Ni-NG	95	550	−0.7 ~ −0.87 (0.17)	110	[93]
Co-N_2	95	570	−0.58 ~ −0.78 (0.2)	/	[94]
NiN-GS	93.2	700	−0.81 (/)	138.5	[95]
AD-Sn/N-C	91	490	−0.6 (/)	140	[96]
Fe^{3+}-N-C	>90%	340	−0.45 (/)	64	[25]

Table S4 Peak positions and the corresponding assignments from in situ ATR-SEIRAS spectra [26,97–103].

Wavenumber (cm^{-1})	Assignment	Substance or group
1260	δ(O–H) deformation [97–99]	*COOH
1365–1390	ν(C–O) stretching [26,97,98]	
1656–1660	ν(C=O) stretching [97,100,101]	
1643	δ(H–O–H) bending [97,99,102]	H_2O
2364	ν_{as}(O=C=O) stretching [26,97,103]	CO_2

References

1. Kresse G, Furthmuller J. Efficiency of ab-initio total energy calculations for metals and semiconductors using a plane-wave basis set. Computational Materials Science, 1996, 6(1): 15–50
2. Kresse G, Furthmuller J. Efficient iterative schemes for ab initio total-energy calculations using a plane-wave basis set. Physical Review B, 1996, 54(16): 11169–11186
3. Perdew J P, Burke K, Ernzerhof M. Generalized gradient approximation made simple. Physical Review Letters, 1996, 77(18): 3865–3868
4. Kresse G, Joubert D. From ultrasoft pseudopotentials to the projector augmented-wave method. Physical Review B, 1999, 59(3): 1758–1775
5. Dudarev S L, Botton G A, Savrasov S Y, Humphreys C J, Sutton A P. Electron-energy-loss spectra and the structural stability of nickel oxide: An LSDA+U study. Physical Review B, 1998, 57(3): 1505–1509
6. Xu H, Cheng D, Cao D, Zeng X C. A universal principle for a rational design of single-atom electrocatalysts. Nature Catalysis, 2018, 1(5): 339–348
7. Grimme S, Antony J, Ehrlich S, Krieg H. A consistent and accurate ab initio parametrization of density functional dispersion correction (DFT-D) for the 94 elements H-Pu. The Journal of Chemical Physics, 2010, 132(15): 154104
8. Zhang H, Li J, Xi S, Du Y, Hai X, Wang J, Xu H, Wu G, Zhang J, Lu J, Wang J. A graphene-supported single-atom FeN_5 catalytic site for efficient electrochemical CO_2 reduction. Angewandte Chemie, 2019, 58(42): 14871–14876
9. Li J, Mao S, Hou Y, Lei L, Yuan C. 3D edge-enriched Fe_3C@C nanocrystals with a core-shell structure grown on reduced graphene oxide networks for efficient oxygen reduction reaction. ChemSusChem, 2018, 11(18): 3292–3298
10. Zhang W, Yin J, Sun M, Wang W, Chen C, Altunkaya M, Emwas A H, Han Y, Schwingenschlogl U, Alshareef H N. Direct pyrolysis of supermolecules: An ultrahigh edge-nitrogen doping strategy of carbon

anodes for potassium-ion batteries. Advanced Materials, 2020, 32(25): 2000732

11. Deng D H, Yu L, Chen X Q, Wang G X, Jin L, Pan X L, Deng J, Sun G Q, Bao X H. Iron encapsulated within pod-like carbon nanotubes for oxygen reduction reaction. Angewandte Chemie, 2013, 52(1): 371–375
12. Zutic I, Fabian J, Das Sarma S. Spintronics: Fundamentals and applications. Reviews of Modern Physics, 2004, 76(2): 323–410
13. Zagal J H, Bedioui F, Dodelet J P. N_4-Macrocyclic Metal Complexes. New York: Springer, 2006, 47–48
14. Kramm U I, Herranz J, Larouche N, Arruda T M, Lefevre M, Jaouen F, Bogdanoff P, Fiechter S, Abs-Wurmbach I, Mukerjee S, Dodelet J P. Structure of the catalytic sites in Fe/N/C-catalysts for O_2-reduction in PEM fuel cells. Physical Chemistry Chemical Physics, 2012, 14(33): 11673–11688
15. Hossain M D, Liu Z, Zhuang M, Yan X, Xu G L, Gadre C A, Tyagi A, Abidi I H, Sun C J, Wong H, Guda A, Hao Y, Pan X, Amine K, Luo Z. Rational design of graphene-supported single atom catalysts for hydrogen evolution reaction. Advanced Energy Materials, 2019, 9(10): 1803689
16. Gong L, Zhang D, Lin C Y, Zhu Y, Shen Y, Zhang J, Han X, Zhang L, Xia Z. Catalytic mechanisms and design principles for single-atom catalysts in highly efficient CO_2 conversion. Advanced Energy Materials, 2019, 9(44): 1902625
17. Jiang W J, Gu L, Li L, Zhang Y, Zhang X, Zhang L J, Wang J Q, Hu J S, Wei Z, Wan L J. Understanding the high activity of Fe-N-C electrocatalysts in oxygen reduction: Fe/Fe_3C nanoparticles boost the activity of Fe-N_x. Journal of the American Chemical Society, 2016, 138(10): 3570–3578
18. Cheng Q, Mao K, Ma L, Yang L, Zou L, Zou Z, Hu Z, Yang H. Encapsulation of iron nitride by Fe-N-C shell enabling highly efficient electroreduction of CO_2 to CO. ACS Energy Letters, 2018, 3(5): 1205–1211
19. Wang H, Yin F X, Liu N, Kou R H, He X B, Sun C J, Chen B H, Liu D J, Yin H Q. Engineering Fe-Fe_3C@Fe-N-C active sites and hybrid structures from dual metal-organic frameworks for oxygen reduction reaction in H_2-O_2 fuel cell and Li-O_2 battery. Advanced Functional Materials, 2019, 29(23): 1901531
20. Hu J, Wang S, Yu J, Nie W, Sun J, Wang S. Duet Fe_3C and FeN_x sites for H_2O_2 generation and activation toward enhanced electro-Fenton performance in wastewater treatment. Environmental Science & Technology, 2021, 55(2): 1260–1269
21. Wu Z Y, Xu X X, Hu B C, Liang H W, Lin Y, Chen L F, Yu S H. Iron carbide nanoparticles encapsulated in mesoporous Fe-N-doped carbon nanofibers for efficient electrocatalysis. Angewandte Chemie, 2015, 54(28): 8179–8183
22. Cui X, Gao L, Lei S, Liang S, Zhang J, Sewell C D, Xue W, Liu Q, Lin Z, Yang Y. Simultaneously Crafting single-atomic fe sites and graphitic layer-wrapped Fe_3C nanoparticles encapsulated within mesoporous carbon tubes for oxygen reduction. Advanced Functional Materials, 2021, 31(10): 2009197
23. Hu Y, Jensen J O, Zhang W, Cleemann L N, Xing W, Bjerrum N J, Li Q. Hollow spheres of iron carbide nanoparticles encased in graphitic layers as oxygen reduction catalysts. Angewandte Chemie, 2014, 53(14): 3675–3679

24. Wang Q, Lei Y, Chen Z, Wu N, Wang Y, Wang B, Wang Y. Fe/Fe$_3$C@C nanoparticles encapsulated in N-doped graphene-CNTs framework as an efficient bifunctional oxygen electrocatalyst for robust rechargeable Zn-air batteries. Journal of Materials Chemistry A, 2018, 6(2): 516–526
25. Gu J, Hsu C S, Bai L, Chen H M, Hu X. Atomically dispersed Fe^{3+} sites catalyze efficient CO$_2$ electroreduction to CO. Science, 2019, 364(6445): 1091–1094
26. Zhu S, Jiang B, Cai W B, Shao M. Direct observation on reaction intermediates and the role of bicarbonate anions in CO$_2$ electrochemical reduction reaction on Cu surfaces. Journal of the American Chemical Society, 2017, 139(44): 15664–15667
27. Szymanski H A. Progress in Infrared Spectroscopy. New York: Springer, 1962, 285
28. Günzler H, Gremlich H U. IR Spectroscopy: An Introduction. Weinheim: Wiley, 2002, 14–16
29. Rankin D W H, Mitzel N W, Morrison C A. Structural Methods in Molecular Inorganic Chemistry. Chichester: Wiley, 2013, 237–238
30. Wang X, Xie J, Ghausi M A, Lv J, Huang Y, Wu M, Wang Y, Yao J. Rechargeable Zn-CO$_2$ electrochemical cells mimicking two-step photosynthesis. Advanced Materials, 2019, 31(17): 1807807
31. Stoner E C. Collective electron ferromagnetism. Proceedings of the Royal Society A, 1938, 165(922): 372–414
32. Stöhr J, Siegmann H C. Magnetism: From Fundamentals to Nanoscale Dynamics. Berlin: Springer, 2006, 218
33. Slater J C. The ferromagnetism of nickel. Physical Review, 1936, 49(7): 537–545
34. Harrison W A. Electronic Structure and the Properties of Solids: The Physics of the Chemical Bond. New York: Dover Publications, 1989, 520–525
35. Stöhr J, Siegmann H C. Magnetism: From Fundamentals to Nanoscale Dynamics. Berlin: Springer, 2006, 235–240
36. White R M. Quantum Theory of Magnetism: Magnetic Properties of Materials. Berlin: Springer, 2007, 177–186
37. Marder M P. Condensed Matter Physics. Hoboken: Wiley, 2010, 811–813
38. Shao Y, Pang R, Shi X. Stability of two-dimensional iron carbides suspended across graphene pores: First-principles particle swarm optimization. Journal of Physical Chemistry C, 2015, 119(40): 22954–22960
39. Haugen H, Huertas-Hernando D, Brataas A. Spin transport in proximity-induced ferromagnetic graphene. Physical Review B, 2008, 77(11): 115406
40. Semenov Y G, Zavada J M, Kim K W. Magnetoresistance in bilayer graphene via ferromagnet proximity effects. Physical Review B, 2008, 77(23): 235415
41. Lazic P, Sipahi G M, Kawakami R K, Zutic I. Graphene spintronics: Spin injection and proximity effects from first principles. Physical Review B, 2014, 90(8): 085429
42. Wang Z, Tang C, Sachs R, Barlas Y, Shi J. Proximity-induced ferromagnetism in graphene revealed by the anomalous hall effect. Physical Review Letters, 2015, 114(1): 016603

43. Han W, Kawakami R K, Gmitra M, Fabian J. Graphene spintronics. Nature Nanotechnology, 2014, 9(10): 794–807
44. Zutic I, Matos-Abiague A, Scharf B, Dery H, Belashchenko K. Proximitized materials. Materials Today, 2019, 22: 85–107
45. Dedkov Y S, Fonin M, Ruediger U, Laubschat C. Rashba effect in the graphene/Ni(111) system. Physical Review Letters, 2008, 100(10): 107602
46. Weser M, Rehder Y, Horn K, Sicot M, Fonin M, Preobrajenski A B, Voloshina E N, Goering E, Dedkov Y S. Induced magnetism of carbon atoms at the graphene/Ni(111) interface. Applied Physics Letters, 2010, 96(1): 012504
47. Yang H X, Hallal A, Terrade D, Waintal X, Roche S, Chshiev M. Proximity effects induced in graphene by magnetic insulators: First-principles calculations on spin filtering and exchange-splitting gaps. Physical Review Letters, 2013, 110(4): 046603
48. Giuliani G F, Vignale G. Quantum Theory of the Electron Liquid. New York: Cambridge University Press, 2005, 32–36
49. Stöhr J, Siegmann H C. Magnetism: From Fundamentals to Nanoscale Dynamics. Berlin: Springer, 2006, 175–186
50. Gong C, Lee G, Shan B, Vogel E M, Wallace R M, Cho K. First-principles study of metal-graphene interfaces. Journal of Applied Physics, 2010, 108(12): 123711
51. Sakai S, Majumdar S, Popov Z I, Avramov P V, Entani S, Hasegawa Y, Yamada Y, Huhtinen H, Naramoto H, Sorokin P B, Yamauchi Y. Proximity-induced spin polarization of graphene in contact with half-metallic manganite. ACS Nano, 2016, 10(8): 7532–7541
52. Sakai S, Erohin S V, Popov Z I, Haku S, Watanabe T, Yamada Y, Entani S, Li S, Avramov P V, Naramoto H, Ando K, Sorokin P B, Yamauchi Y. Dirac cone spin polarization of graphene by magnetic insulator proximity effect probed with outermost surface spin spectroscopy. Advanced Functional Materials, 2018, 28(20): 1800462
53. Novoselov K S, Geim A K, Morozov S V, Jiang D, Katsnelson M I, Grigorieva I V, Dubonos S V, Firsov A A. Two-dimensional gas of massless Dirac fermions in graphene. Nature, 2005, 438(7065): 197–200
54. Tombros N, Jozsa C, Popinciuc M, Jonkman H T, Van Wees B J. Electronic spin transport and spin precession in single graphene layers at room temperature. Nature, 2007, 448(7153): 571–574
55. Zagal J H, Bedioui F, Dodelet J P. N_4-Macrocyclic Metal Complexes. New York: Springer, 2006, 41
56. Ramaswamy N, Tylus U, Jia Q, Mukerjee S. Activity descriptor identification for oxygen reduction on nonprecious electrocatalysts: Linking surface science to coordination chemistry. Journal of the American Chemical Society, 2013, 135(41): 15443–15449
57. Mun Y, Lee S, Kim K, Kim S, Lee S, Han J W, Lee J. Versatile strategy for tuning ORR activity of a single Fe-N_4 site by controlling electron-withdrawing/donating properties of a carbon plane. Journal of the American Chemical Society, 2019, 141(15): 6254–6262

58. Kettle S F A. Physical Inorganic Chemistry: A Coordination Chemistry Approach. Berlin: Springer, 1996, 103–104

59. Stöhr J, Siegmann H C. Magnetism: From Fundamentals to Nanoscale Dynamics. Berlin: Springer, 2006, 209–211

60. Rauk A. Orbital Interaction Theory of Organic Chemistry. New York: Wiley, 2001, 52

61. Fleming I. Molecular Orbitals and Organic Chemical Reactions. Chichester: Wiley, 2010, 24–25

62. Freund H J, Roberts M W. Surface chemistry of carbon dioxide. Surface Science Reports, 1996, 25(8): 225–273

63. Demtröder W. Atoms, Molecules and Photons: An Introduction to Atomic-, Molecular- and Quantum Physics. Berlin: Springer, 2018, 361–362

64. Hammer B, Norskov J K. Why gold is the noblest of all the metals. Nature, 1995, 376(6537): 238–240

65. Hammer B, Norskov J K. Electronic factors determining the reactivity of metal surfaces. Surface Science, 1995, 343(3): 211–220

66. Hammer B, Norskov J K: Theoretical surface science and catalysis: Calculations and concepts, Gates B C, Knozinger H, editors, Advances in Catalysis, Vol 45: Impact of Surface Science on Catalysis, 2000, 71–129.

67. Hoffmann R. A chemical and theoretical way to look at bonding on surfaces. Reviews of Modern Physics, 1988, 60(3): 601–628

68. Whitten J L, Yang H. Theory of chemisorption and reactions on metal surfaces. Surface Science Reports, 1996, 24(3–4): 59–124

69. Ballhausen C J, Gray H B. Molecular Orbital Theory: An Introductory Lecture Note and Reprint Volume. New York: W. A. Benjamin, 1965, 24–26

70. Ballhausen C J, Gray H B. Molecular Orbital Theory: An Introductory Lecture Note and Reprint Volume. New York: W. A. Benjamin, 1965, 17

71. Demtröder W. Atoms, Molecules and Photons: An Introduction to Atomic-, Molecular- and Quantum Physics. Berlin: Springer, 2018, 309

72. Brown T L, Lemay H E, Bursten B E, Murphy C J, Woodward P M, Stoltzfus M W. Chemistry: The Central Science. London: Pearson, 2018, 412–415

73. Demtröder W. Atoms, Molecules and Photons: An Introduction to Atomic-, Molecular- and Quantum Physics. Berlin: Springer, 2018, 321

74. Jiao Y, Zheng Y, Jaroniec M, Qiao S Z. Origin of the electrocatalytic oxygen reduction activity of graphene-based catalysts: A roadmap to achieve the best performance. Journal of the American Chemical Society, 2014, 136(11): 4394–4403

75. Tao H B, Fang L W, Chen J Z, Yang H B, Gao J J, Miao J W, Chen S L, Liu B. Identification of surface reactivity descriptor for transition metal oxides in oxygen evolution reaction. Journal of the American Chemical Society, 2016, 138(31): 9978–9985

76. Ballhausen C J, Gray H B. Molecular Orbital Theory: An Introductory Lecture Note and Reprint Volume.

New York: W. A. Benjamin, 1965, 23

77. Ren X, Wu T Z, Sun Y M, Li Y, Xian G Y, Liu X H, Shen C M, Gracia J, Gao H J, Yang H T, Xu Z C J. Spin-polarized oxygen evolution reaction under magnetic field. Nature Communications, 2021, 12(1): 2608
78. Wu T Z, Ren X, Sun Y M, Sun S N, Xian G Y, Scherer G G, Fisher A C, Mandler D, Ager J W, Grimaud A, Wang J L, Shen C M, Yang H T, Gracia J, Gao H J, Xu Z C J. Spin pinning effect to reconstructed oxyhydroxide layer on ferromagnetic oxides for enhanced water oxidation. Nature Communications, 2021, 12(1): 3634
79. Zhang X, Li X Q, Zhang D, Su N Q, Yang W T, Everitt H O, Liu J. Product selectivity in plasmonic photocatalysis for carbon dioxide hydrogenation. Nature Communications, 2017, 8: 14542
80. Lin S C, Hsu C S, Chiu S Y, Liao T Y, Chen H M. Edgeless Ag-Pt bimetallic nanocages: In situ monitor plasmon-induced suppression of hydrogen peroxide formation. Journal of the American Chemical Society, 2017, 139(6): 2224–2233
81. Yang J H, Guo Y Z, Jiang R B, Qin F, Zhang H, Lu W Z, Wang J F, Yu J C. High-efficiency "working-in-tandem" nitrogen photofixation achieved by assembling plasmonic gold nanocrystals on ultrathin titania nanosheets. Journal of the American Chemical Society, 2018, 140(27): 8497–8508
82. Schmickler W, Santos E. Interfacial Electrochemistry. Berlin: Springer, 2010, 90–96
83. Jackson M N, Surendranath Y. Molecular control of heterogeneous electrocatalysis through graphite conjugation. Accounts of Chemical Research, 2019, 52(12): 3432–3441
84. Jackson M N, Oh S, Kaminsky C J, Chu S B, Zhang G, Miller J T, Surendranath Y. Strong electronic coupling of molecular sites to graphitic electrodes via pyrazine conjugation. Journal of the American Chemical Society, 2018, 140(3): 1004–1010
85. Jackson M N, Kaminsky C J, Oh S, Melville J F, Surendranath Y. Graphite conjugation eliminates redox intermediates in molecular electrocatalysis. Journal of the American Chemical Society, 2019, 141(36): 14160–14167
86. Pan Y, Lin R, Chen Y, Liu S, Zhu W, Cao X, Chen W, Wu K, Cheong W C, Wang Y, Zheng L, Luo J, Lin Y, Liu Y, Liu C, Li J, Lu Q, Chen X, Wang D, Peng Q, Chen C, Li Y. Design of single-atom Co-N_5 catalytic site: A robust electrocatalyst for CO_2 reduction with nearly 100% CO selectivity and remarkable stability. Journal of the American Chemical Society, 2018, 140(12): 4218–4221
87. Zhang B, Zhang J, Shi J, Tan D, Liu L, Zhang F, Lu C, Su Z, Tan X, Cheng X, Han B, Zheng L, Zhang J. Manganese acting as a high-performance heterogeneous electrocatalyst in carbon dioxide reduction. Nature Communications, 2019, 10(1): 2980
88. Yang H B, Hung S F, Liu S, Yuan K, Miao S, Zhang L, Huang X, Wang H Y, Cai W, Chen R, Gao J, Yang X, Chen W, Huang Y, Chen H M, Li C M, Zhang T, Liu B. Atomically dispersed Ni(I) as the active site for electrochemical CO_2 reduction. Nature Energy, 2018, 3(2): 140–147
89. Zheng W, Wang Y, Shuai L, Wang X, He F, Lei C, Li Z, Yang B, Lei L, Yuan C, Qiu M, Hou Y, Feng X. Highly boosted reaction kinetics in carbon dioxide electroreduction by surface-introduced electronegative

dopants. Advanced Functional Materials, 2021, 31(15): 2008146

90. Wang T, Sang X, Zheng W, Yang B, Yao S, Lei C, Li Z, He Q, Lu J, Lei L, Dai L, Hou Y. Gas diffusion strategy for inserting atomic iron sites into graphitized carbon supports for unusually high-efficient CO_2 electroreduction and high-performance Zn-CO_2 batteries. Advanced Materials, 2020, 32(29): 2002430
91. Su P, Iwase K, Nakanishi S, Hashimoto K, Kamiya K. Nickel-nitrogen-modified graphene: An efficient electrocatalyst for the reduction of carbon dioxide to carbon monoxide. Small, 2016, 12(44): 6083–6089
92. Yang F, Song P, Liu X, Mei B, Xing W, Jiang Z, Gu L, Xu W. Highly efficient CO_2 electroreduction on ZnN_4-based single-atom catalyst. Angewandte Chemie, 2018, 57(38): 12303–12307
93. Jiang K, Siahrostami S, Zheng T, Hu Y, Hwang S, Stavitski E, Peng Y, Dynes J, Gangisetty M, Su D, Attenkofer K, Wang H. Isolated Ni single atoms in graphene nanosheets for high-performance CO_2 reduction. Energy & Environmental Science, 2018, 11(4): 893–903
94. Wang X, Chen Z, Zhao X, Yao T, Chen W, You R, Zhao C, Wu G, Wang J, Huang W, Yang J, Hong X, Wei S, Wu Y, Li Y. Regulation of coordination number over single Co sites: Triggering the efficient electroreduction of CO_2. Angewandte Chemie, 2018, 57(7): 1944–1948
95. Jiang K, Siahrostami S, Akey A J, Li Y, Lu Z, Lattimer J, Hu Y, Stokes C, Gangishetty M, Chen G, Zhou Y, Hill W, Cai W B, Bell D, Chan K, Norskov J K, Cui Y, Wang H. Transition-metal single atoms in a graphene shell as active centers for highly efficient artificial photosynthesis. Chem, 2017, 3(6): 950–960
96. Zhao Y, Liang J, Wang C, Ma J, Wallace G G. Tunable and efficient tin modified nitrogen-doped carbon nanofibers for electrochemical reduction of aqueous carbon dioxide. Advanced Energy Materials, 2018, 8(10): 1702524
97. Firet N J, Smith W A. Probing the reaction mechanism of CO_2 electroreduction over Ag films via operando infrared spectroscopy. ACS Catalysis, 2017, 7(1): 606–612
98. Xia X H, Liess H D, Iwasita T. Early stages in the oxidation of ethanol at low index single crystal platinum electrodes. Journal of Electroanalytical Chemistry, 1997, 437(1–2): 233–240
99. Garand E, Wende T, Goebbert D J, Bergmann R, Meijer G, Neumark D M, Asmis K R. Infrared spectroscopy of hydrated bicarbonate anion clusters: $HCO_3^-(H_2O)_{1-10}$. Journal of the American Chemical Society, 2010, 132(2): 849–856
100. Lee S J, Han S W, Yoon M, Kim K. Adsorption characteristics of 4-dimethylaminobenzoic acid on silver and titania: Diffuse reflectance infrared Fourier transform spectroscopy study. Vibrational Spectroscopy, 2000, 24(2): 265–275
101. Han S W, Ha T H, Kim C H, Kim K. Self-assembly of anthraquinone-2-carboxylic acid on silver: Fourier transform infrared spectroscopy, ellipsometry, quartz crystal microbalance, and atomic force microscopy study. Langmuir, 1998, 14(21): 6113–6120
102. Mizaikoff B. Waveguide-enhanced mid-infrared chem/bio sensors. Chemical Society Reviews, 2013, 42(22): 8683–8699
103. Nikolic B Z, Huang H, Gervasio D, Lin A, Fierro C, Adzic R R, Yeager E B. Electroreduction of carbon

dioxide on platinum single crystal electrodes: electrochemical and in situ FTIR studies. Journal of Electroanalytical Chemistry, 1990, 295(1–2): 415–423